0830-L-02

NAS1.29/3-2:99-04

NASA Tech Briefs

COMPLETE

National Aeronautics and
Space Administration

Electronic Components and Circuits

Electronic Systems

Physical Sciences

Materials

Computer Programs

Mechanics

Machinery

Fabrication Technology

Mathematics and Information Sciences

Life Sciences

99-04

April 1999

99-021936

INTRODUCTION

Tech Briefs are short announcements of innovations originating from research and development activities of the National Aeronautics and Space Administration. They emphasize information considered likely to be transferable across industrial, regional, or disciplinary lines and are issued to encourage commercial application.

Availability of NASA Tech Briefs and TSPs

Requests for individual Tech Briefs or for Technical Support Packages (TSPs) announced herein should be addressed to

National Technology Transfer Center
Telephone No. **(800) 678-6882** or via World Wide Web at **www2.nttc.edu/leads/**

Please reference the control numbers appearing at the end of each Tech Brief. Information on NASA's Commercial Technology Team, its documents, and services is also available at the same facility or on the World Wide Web at **www.nctn.hq.nasa.gov**.

Commercial Technology Offices and Patent Counsels are located at NASA field centers to provide technology-transfer access to industrial users. Inquiries can be made by contacting NASA field centers and program offices listed below.

NASA Field Centers and Program Offices

Ames Research Center
Carolina Blake
(650) 604-0893 or
cblake@mail.arc.nasa.gov

Dryden Flight Research Center
Lee Duke
(805) 258-3802 or
lee.duke@dfrc.nasa.gov

Goddard Space Flight Center
George Alcorn
(301) 286-5810 or
galcorn@gsfc.nasa.gov

Jet Propulsion Laboratory
Merle McKenzie
(818) 354-2577 or
merle.mckenzie@ccmail.jpl.nasa.gov

Johnson Space Center
Hank Davis
(281) 483-0474 or
hdavis@gp101.jsc.nasa.gov

John F. Kennedy Space Center
Gale Allen
(407) 867-6626 or
galeallen-1@ksc.nasa.gov

Langley Research Center
Dr. Joseph S. Heyman
(804) 864-6006 or
j.s.heyman@larc.nasa.gov

Lewis Research Center
Larry Viterna
(216) 433-3484 or
cto@lerc.nasa.gov

George C. Marshall Space Flight Center
Sally Little
(256) 544-4266 or
sally.little@msfc.nasa.gov

John C. Stennis Space Center
Kirk Sharp
(228) 688-1929 or
ksharp@ssc.nasa.gov

NASA Program Offices
At NASA Headquarters there are seven major program offices that develop and oversee technology projects of potential interest to industry:

Carl Ray
Small Business Innovation Research Program (SBIR) & Small Business Technology Transfer Program (STTR)
(202) 358-4652 or
cray@mail.hq.nasa.gov

Dr. Robert Norwood
Office of Aeronautics and Space Transportation Technology (Code R)
(202) 358-2320 or
rnorwood@mail.hq.nasa.gov

John Mulcahy
Office of Space Flight (Code MP)
(202) 358-1401 or
jmulcahy@mail.hq.nasa.gov

Gerald Johnson
Office of Aeronautics (Code R)
(202) 358-4711 or
g_johnson@aeromail.hq.nasa.gov

Bill Smith
Office of Space Science (Code S)
(202) 358-2473 or
wsmith@sm.ms.ossa.hq.nasa.gov

Roger Crouch
Office of Microgravity Science Applications (Code U)
(202) 358-0689 or
rcrouch@hq.nasa.gov

Granville Paules
Office of Mission to Planet Earth (Code Y)
(202) 358-0706 or
gpaules@mtpe.hq.nasa.gov

BLANK PAGE

NASA TechBriefs

National Aeronautics and
Space Administration

April 1999
99-04

5 Electronic Components and Circuits

15 Electronic Systems

19 Physical Sciences

29 Materials

37 Mechanics

41 Machinery

47 Fabrication Technology

51 Mathematics and Information Sciences

This document was prepared under the sponsorship of the National Aeronautics and Space Administration. Neither the United States Government nor any person acting on behalf of the United States Government assumes any liability resulting from the use of the information contained in this document, or warrants that such use will be free from privately owned rights.

BLANK PAGE

Electronic Components and Circuits

Hardware, Techniques, and Processes

7 $In_xGa_{1-x}P/In_xGa_{1-x}As$-on-Ge Solar Photovoltaic Cells
8 Broad-Band $GaAs/Al_xGa_{1-x}As$ QWIPs
9 Vertical-Bloch-Line Memories Containing Stacked Chips
9 Solar Heating of Batteries in Cold Environments
10 Circuit for Automatic Tunneling-Controlled Golay Cell
11 Interlayer Stripline Transition
12 High-Performance HgCdTe Detectors for Remote Sensing: Part 1
13 High-Performance HgCdTe Detectors for Remote Sensing: Part 2
13 Improvements in Fabrication of HgCdTe Photodetectors

BLANK PAGE

$In_xGa_{1-x}P/In_xGa_{1-x}As$-on-Ge Solar Photovoltaic Cells

Energy-conversion efficiencies are expected to exceed those of other known solar cells.

Lewis Research Center, Cleveland, Ohio

Monolithic, tandem two-junction $In_xGa_{1-x}P/In_xGa_{1-x}As$-on-Ge solar photovoltaic cells are being developed. The cells are designed to be used with solar concentrators to generate electric power aboard spacecraft. The theoretically achievable energy-conversion efficiency of these cells under air-mass-zero (AM0) conditions and 10× concentrated solar illumination is about 33 percent. In comparison with other known dual-junction photovoltaic cells, the proposed cells would feature highest conversion efficiency and the highest specific power. The cost per unit of power of these cells would be less than the costs per unit power of GaAs and InGaP/GaAs cells. With modifications, the cells might offer similar advantages in terrestrial applications.

To approach the theoretical efficiency, it is necessary to configure a tandem cell with an optimal combination of bandgaps. In the present case, this translates to putting the $In_xGa_{1-x}P$ cell (which has a bandgap of 1.65 to 1.7 eV) on top and the $In_xGa_{1-x}As$ cell (which has a bandgap of about 1.1 eV) on the bottom. Although the $In_xGa_{1-x}As$ and $In_xGa_{1-x}P$ are lattice-matched to each other, they are lattice-mismatched to all available substrate materials. Heretofore, the lack of a lattice-matched substrate material has impeded the realization of tandem cells with optimal bandgaps.

The approach taken in the present development effort is to form the tandem cell structure on a Ge substrate by organo-metallic vapor-phase epitaxy (OMVPE), using a lattice-grading technique to overcome the lattice mismatch. In addition, Ge offers the advantage of being inexpensive and rugged.

The figure depicts the proposed cell structure. The first layer deposited on the Ge substrate would be a buffer layer of GaAs, which is lattice-matched to Ge. Then a stack of $In_xGa_{1-x}As$ layers with increasing In contents would be deposited. The final InGaAs layer would have a total In content of about 23 atomic percent, as needed to obtain a bandgap of 1.1 eV for the lower cell. The subsequent lattice-matched layers (deposited without additional buffer layers) would include (1) $In_xGa_{1-x}As$ tunnel-junction layers, $In_xGa_{1-x}As$ layers of the bottom cell, more tunnel-junction layers, an AlInP window layer (bandgap 2.1 eV), $In_xGa_{1-x}P$ layers for the top cell, and a top window layer of AlInP. An antireflection coating and a contact grid would be applied to the top window layer, and a contact layer would be formed on the bottom of the substrate.

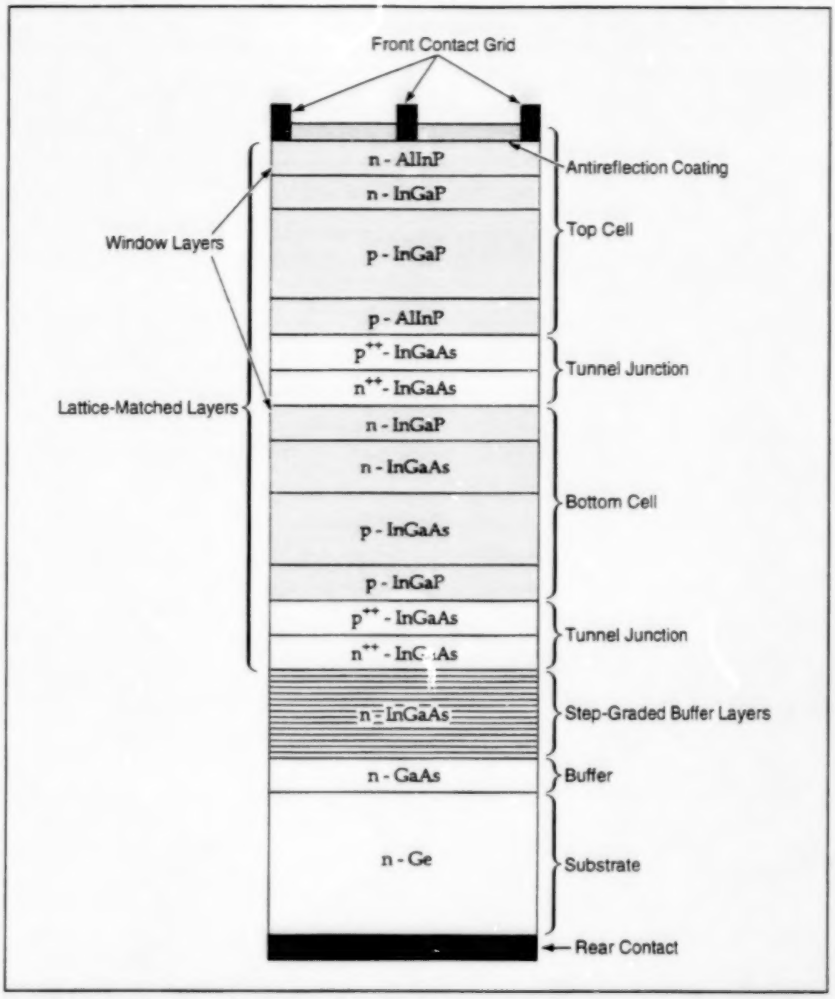

The **Proposed $In_xGa_{1-x}As/In_xGa_{1-x}P$-on-Ge Tandem Cell Structure** is expected to afford unprecedented 1-Sun AM0 energy-conversion efficiency as high as 33 percent.

Because of limitations of time and short-term unavailability of Ge substrates, GaAs substrates were used in initial experiments on the feasibility of OMVPE deposition of lattice-mismatched $In_xGa_{1-x}As$. The experiments proved successful in that the uppermost $In_xGa_{1-x}As$ layers had the desired 1.1-eV bandgaps and the densities of dislocations in these layers were below the detection limit of transmission electron microscopy ($10^7/cm^2$).

For other experiments to demonstrate the feasibility of the lower-cell design and part of the upper-cell design, $In_xGa_{1-x}As$ cells with $In_xGa_{1-x}P$ window layers, without antireflection coatings, and with 19-percent front grid coverage were fabricated on GaAs substrates. In the experiments, the best of these cells, with bandgaps of 1.07 and 1.15 eV, exhibited AM0 conversion efficiencies of 10.94 and 11.5 percent, respectively under 1-Sun illumination, and about 12.5 percent under 10-Sun illumination. Estimation of the effects of including antireflection coatings and reducing front grid coverage to a typical value of 5 percent leads to extrapolated 1-Sun AM0 conversion efficiencies of 17.5 and 18.4 percent, respectively. These efficiencies are almost as good as the 1-Sun AM0 efficiencies (about 20 percent) of the best Si cells.

This work was done by Richard W. Hoffman, Jr., Mark A. Stan, and Navid Fatemi of Essential Research, Inc., for

Lewis Research Center. *No further documentation is available.*

Inquiries concerning rights for the commercial use of this invention should be addressed to NASA Lewis Research Center, Commercial Technology Office, Attn: Steve Fedor, Mail Stop 4–8, 21000 Brookpark Road, Cleveland, Ohio 44135. Refer to LEW-16697.

Broad-Band GaAs/$Al_xGa_{1-x}As$ QWIPs

Quantum wells designed for different pass bands are stacked in repeating sequences.

NASA's Jet Propulsion Laboratory, Pasadena, California

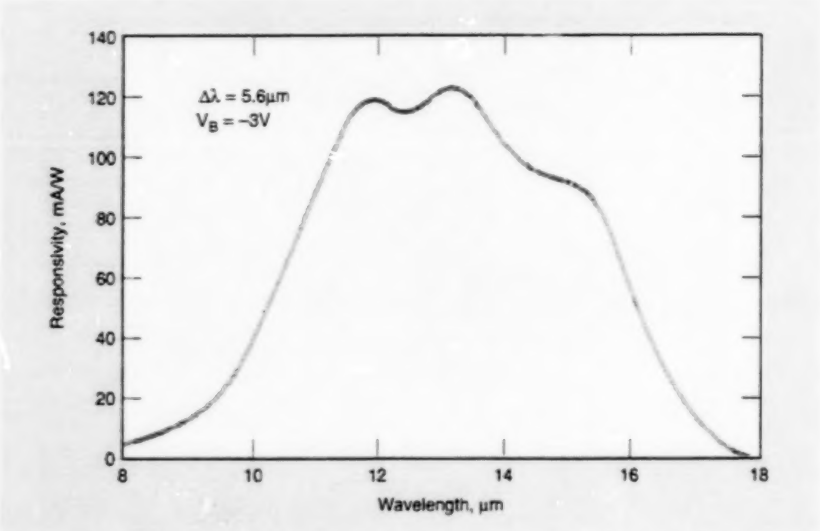

The **Spectral Responsivity of a QWIP** containing repeating sequence of three different wells was much broader than that of a typical older QWIP containing multiple identical wells.

GaAs/$Al_xGa_{1-x}As$ quantum-well infrared photodetectors (QWIPs) with broad-band responses are undergoing development. The broad-band responses are obtained by varying the depths and widths of the wells and the thicknesses of the barriers between the wells, as explained below.

A GaAs/$Al_xGa_{1-x}As$ QWIP contains layers of GaAs (the wells) alternating with layers of $Al_xGa_{1-x}As$ ($0<x<1$) (the barriers). Detection of a photon in a QWIP involves photoexcitation of electrons from the ground to the first excited quantum state of one of the wells. The excited electron can escape from the well and, if a suitable bias voltage is applied, then many such photoelectrons are collected as photocurrent.

Typically, a QWIP is of the bound-to-continuum or the bound-to-quasi-bound type. In the bound-to-continuum type, the first excited state lies above the top of the well. In the bound-to-quasi-bound type, the first excited state lies exactly at the top of the well. Each of these types offers a different advantage; the spectral width of photoresponse is broader in the bound-to-continuum type, while the bound-to-quasi-bound case offers the advantage of a smaller thermionic contribution to dark current.

The height of each barrier, and thus the depth of an adjacent well, is determined by the mole fraction (x) of aluminum. The energy heights of ground and first excited states relative to the tops and bottoms of the wells, plus the spectral responses of QWIPs, are determined by the widths of the wells, the thicknesses and heights of the barriers, and the well-doping densities. These thicknesses and compositions can be chosen by design and implemented with established deposition techniques.

In a typical bound-to-quasi-bound QWIP of older design, all of the wells are of the same width and doping density, and all of the barriers are of the same thickness and the same aluminum content. The spectral width of its photoresponse is about 10 percent of its peak-response wavelength, which can be set at a value between 6 and 20 μm by suitable choice of layer thicknesses and x.

A device with broader spectral response can be constructed by stacking different quantum wells in a repeating sequence. Each sequence contains several quantum wells; the thicknesses and compositions of the barrier and well layers within each sequence can be tailored to optimize each well for a different pass band that partly overlaps one or more pass band(s) of the other wells in the sequence. The net effect of the multiple partial overlaps is a broader overall pass band for the QWIP device as a whole.

An experimental device of this type was made with 35 repeating three-well sequences. The wells in each sequence were designed for peak responses at wavelengths of 13.5, 14.3, and 15.5 μm, respectively. The measured spectral response of this device (see figure) was found to be about 4 times as broad as that of a typical bound-to-quasi-bound QWIP of older design for the same nominal peak wavelength.

This work was done by Sumith Bandara and Sarath Gunapala of Caltech for **NASA's Jet Propulsion Laboratory**. *Further information is contained in a TSP [see page 1].*

In accordance with Public Law 96-517, the contractor has elected to retain title to this invention. Inquiries concerning rights for its commercial use should be addressed to

Technology Reporting Office
JPL
Mail Stop 122-116
4800 Oak Grove Drive
Pasadena, CA 91109
(818) 354-2240

Refer to NPO-20319, volume and number of this NASA Tech Briefs *issue, and the page number.*

Vertical-Bloch-Line Memories Containing Stacked Chips

VBL memory chips would be stacked in alternation with bias magnets.

NASA's Jet Propulsion Laboratory, Pasadena, California

Vertical-Bloch-line (VBL) memory devices of a proposed type would include stacks of VBL memory chips plus other components (see figure). Each chip would be square, approximately 15 mm on each side. Each chip would have two input/output (I/O) lines connected to 16 I/O pads on each of two opposite edges. All the chips in a stack would be oriented with their I/O pads on the same two opposite faces of the stack. Buses for connection to external circuitry would be positioned to cross the chip edges on these two faces, making contact with the I/O pads.

As specified in a preliminary design, the core of each VBL memory chip would comprise 512 VBL storage loops with 2,048 bits per loop. Thus, each chip could store 512 × 2,048 = 1,048,576 bits. The storage loops would be embodied by stripe domains stabilized in main grooves 5 μm wide and 1.25 μm deep in a garnet substrate. The bits would be embodied by VBL pairs in the walls of the stripe domains and would be stabilized by grooves 5 μm wide and 0.125 μm deep perpendicular to the main grooves. This design would make it possible to exchange 16 32-bit data with the core in parallel. With refinements in design and fabrication involving primarily the use of readily available 2-μm magnetic-bubble material and narrower features (viz., storage loops and I/O lines 2 μm wide and bit grooves 0.5 μm wide), the storage capacity of a chip of the same size could be increased to about 25 Mb. Then using submicron lithography when the 0.5-μm magnetic-bubble material now undergoing development becomes available, it should be possible to increase the capacity to about 400 Mb per chip.

In addition to I/O drive currents supplied via I/O pads, operation of a VBL chip depends on two spatially uniform magnetic fields perpendicular to the chip plane: a dc magnetic bias field and field oscillating at a frequency of several megahertz for VBL propagation. In a device as proposed, the dc magnetic bias fields would be provided by permanent-magnet plates between the chips and at the ends of each stack. The high-frequency VBL-propagation magnetic field would be generated by use of a coil surrounding the stack.

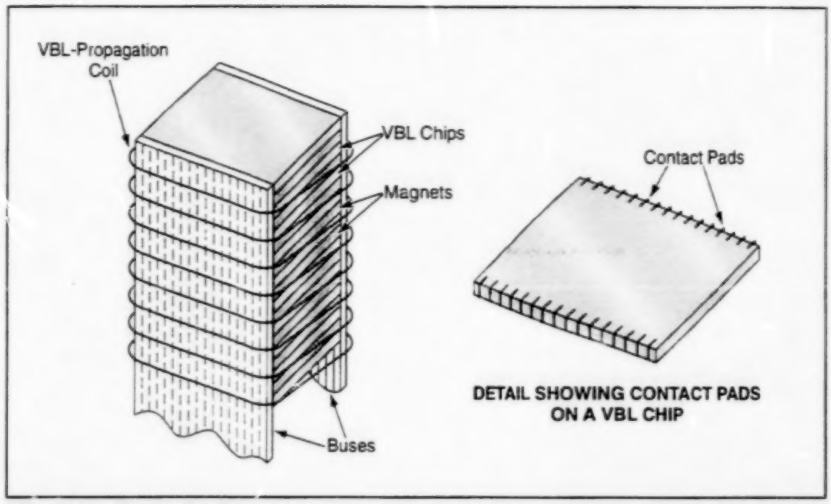

VBL Chips Would Be Stacked to obtain high bit density in a memory device. The general design of devices like this one reflects consideration of manufacturability, yield, biasing, driving, and packaging.

Nonuniformity in the dc magnetic field at the ends of the stack could be reduced to acceptable levels by stacking more magnets at the ends, thickening the end magnets, using high-permeability equalizer plates, bevelling the edges of the magnets to reduce edge fields, and/or the use of a high-permeability sheet housing that would both perform the function of a conventional magnet yoke and act as a shield against externally generated magnetic-field disturbances. The number of windings in the VBL-propagation coil must be large enough to keep the nonuniformity of its magnetic field acceptably small, but not so large that the resulting inductance would be excessive at the operating frequency. The optimum winding density would probably be about 1 turn per chip, except at the ends, where the winding density would have to be doubled to prevent excessive nonuniformity of the magnetic field.

This work was done by Udo Lieneweg of Caltech for **NASA's Jet Propulsion Laboratory**. *For further information, access the Technical Support Package (TSP)* ***free on-line at www.nasatech.com*** *under the category.*

In accordance with Public Law 96-517, the contractor has elected to retain title to this invention. Inquiries concerning rights for its commercial use should be addressed to

Technology Reporting Office
JPL
Mail Stop 122-116
4800 Oak Grove Drive
Pasadena, CA 91109
(818) 354-2240

Refer to NPO-20151, volume and number of this NASA Tech Briefs *issue, and the page number.*

Solar Heating of Batteries in Cold Environments

Heat that would otherwise be rejected would keep batteries at operating temperatures.

NASA's Jet Propulsion Laboratory, Pasadena, California

According to a proposal for small electric-power systems that must operate in cold environments, heat released in the operation of solar photovoltaic arrays with solar concentrators would be utilized to maintain batteries at operating temperatures. The proposal is straightforward and does not impose a requirement for any fundamental new technological developments. The proposal is applicable to secondary batteries, which are charged by use of the photovoltaic arrays.

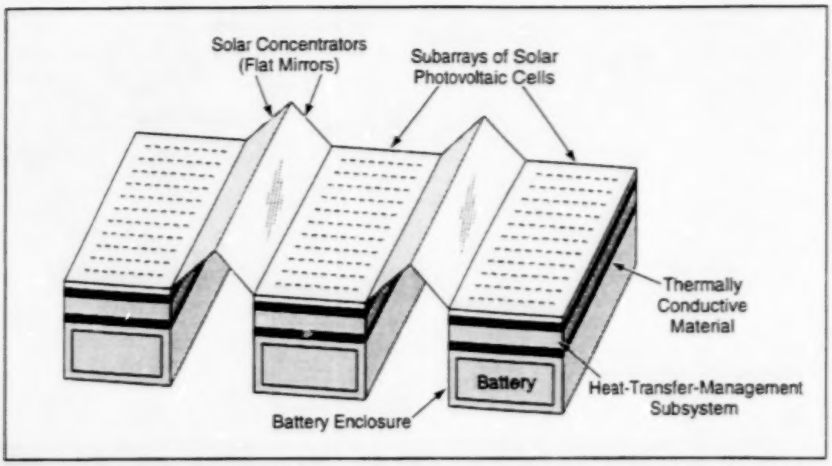

Batteries Would Be Mounted below photovoltaic cells and solar concentrators. Waste heat from the solar concentrators and photovoltaic cells would be used to maintain the batteries at operating temperatures.

Common batteries that contain aqueous electrolytes perform poorly at temperatures below –10 °C, because the electrolytes freeze and/or become viscous, with consequent degradation of ion-transport properties. The low-temperature performances of some lithium primary and lithium-ion secondary batteries have been improved by use of nonaqueous electrolytes, but there remains a problem of what to do in environments colder than their lowest operational temperatures. The proposal offers an alternative solution for batteries of all types.

The typical energy-conversion efficiencies of modern solar photovoltaic cells range from 5 to 25 percent; consequently, most of the solar radiation focused by solar concentrators onto solar photovoltaic cells is converted to heat. It is necessary to remove excess solar heat because the efficiencies of solar photovoltaic cells decrease with increasing temperature. Heretofore, various forms of active and passive cooling have been used to remove heat from solar photovoltaic cells. The basic concept of the proposal is to divert some or all of this heat to the batteries instead of rejecting all of it to the environment.

The figure illustrates an example of how the proposal might be implemented in a system in which the solar concentrators are simple flat mirrors located between subarrays of solar photovoltaic cells. The batteries would be placed behind the subarrays. Preferred configuration might consist of thin type batteries coupled with photovoltaic cells which would be considered to be amenable to a wide range of applications. The batteries would be thermally connected to the subarrays via heat-transfer-management subsystems and layers of heat-conductive material. Depending upon the specific application, the heat-transfer-management subsystems in a given system might contain heat pipes, thermostats, and/or heat reservoirs containing phase-change materials. Phase-change materials could be used to reduce temperature fluctuations. Heat pipes could be used during periods of low insolation to transfer, to the batteries, heat stored previously during peak insolation. Thermostats could be used during peak insolation to break the thermal connections when temperatures exceed a specified value.

The innovations discussed here are formulated concepts, and have not been fully reduced to practice.

This work was done by Julian Blosiu, Marshall Smart, Garry Burdick, and Subbarao Surampudi of Caltech for **NASA's Jet Propulsion Laboratory**. *Further information is contained in a TSP [see page 1].*
NPO-20284

Circuit for Automatic Tunneling-Controlled Golay Cell

Features include low noise, high gain, and low power consumption.

NASA's Jet Propulsion Laboratory, Pasadena, California

An automatic tunneling-controlled, micromachined Golay cell has been implemented in a multichip integrated-circuit module. The module is designed specifically for sensing infrared radiation indicative of the concentration of glucose in blood, but its low noise, high gain, and low power consumption also make it attractive for other infrared-sensing applications.

Numerous micromachined sensors based on the use of electronic feedback control to maintain a constant level of quantum-mechanical tunneling of electrons have been reported in *NASA Tech Briefs*. Particularly relevant was a class of Golay-cell/tunneling-device combinations described in "Micromachined Electron-Tunneling Infrared Detectors" (NPO-18413), in *Laser Tech Briefs*, Vol. 1, No. 1 (September 1993), page 20.

In the present device, the basic principle described above is exploited to measure the pressure on a membrane of a micromachined Golay cell. A bias voltage is applied across a small gap (about 10 Å wide) between two tunneling electrodes, of which one is the membrane in question coated with metal and the other is a tunneling tip. The bias voltage gives rise to a quantum-mechanical-tunneling current of electrons between these electrodes, and the magnitude of this current depends on the size of the gap.

The distance between the membrane and the tunneling tip is controlled by applying a control voltage to an electrostatic-deflection electrode. The circuit adjusts the control voltage to counteract any deviation of the tunneling current from a preset value and thereby maintain the desired constant gap of about 10 Å. The feedback loop that generates the control voltage includes a long-time-constant integrator, the output of which controls the current through a transistor. The voltage drop of this current through a resistor governs the voltage applied to the electrostatic-deflection electrode. The control voltage is a measure of the force needed to prevent deflection of the membrane from the desired constant gap and is thus a measure of the pressure of gas on the membrane, as affected by absorption of infrared radiation in the gas according to the classical Golay-cell principle.

This work was done by Vardkes Victor Boyadzhyan-Sevak of Caltech for **NASA's Jet Propulsion Laboratory**. *Further information is contained in a TSP [see page 1].*

In accordance with Public Law 96-517, the contractor has elected to retain title to this invention. Inquiries concerning rights for its commercial use should be addressed to

Technology Reporting Office
JPL
Mail Stop 122-116
4800 Oak Grove Drive
Pasadena, CA 91109

(818) 354-2240
Refer to NPO-20035, volume and number of this NASA Tech Briefs *issue, and the page number.*

Interlayer Stripline Transition

Elimination of vertical conductive interconnections would ease fabrication.

NASA's Jet Propulsion Laboratory, Pasadena, California

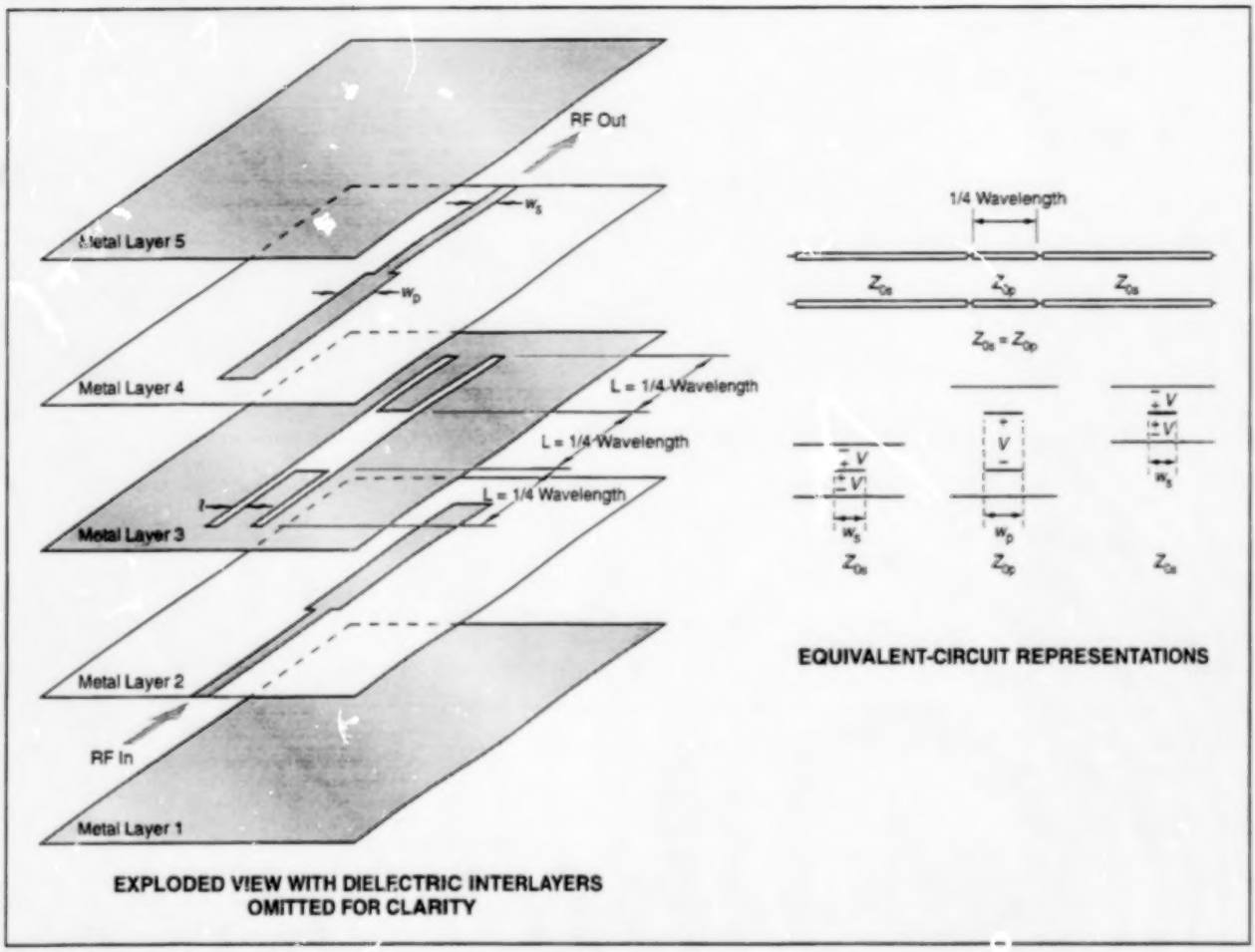

Figure 1. The **Absence of Through-the-Thickness Interconnections** eases fabrication. Interlayer coupling is achieved solely via the interlayer electromagnetic field.

A proposed multilayer metal-film/dielectric-plate laminate would serve as a passive radio-frequency (RF) interlayer stripline transition. This device is designed to provide RF coupling from (a) an input transmission line of the stripline type spanning the first through third metal layers, with characteristic impedance Z_{0s} to (b) an intermediate transmission line of the parallel-line type spanning the first through fifth metal layers, with characteristic impedance $Z_{0p} = Z_{0s}$ to (c) an output transmission line of the stripline type spanning the third through fifth metal layers, with characteristic impedance Z_{0s}.

The main advantage of this device lies in its purely planar geometry. Generally, interlayer stripline coupling is achieved by use of vertical probes; that is, through-the-thickness electrical interconnections, which contribute to difficulty of fabrication. The present design provides for RF coupling via the interlayer electromagnetic field, eliminating the need for vertical probes and thereby easing fabrication.

The basic configuration of the device is illustrated in Figure 1. All of the dielectric layers (not shown) between the metal layers are assumed to be of equal thickness h and equal relative permittivity ε_r. The quarter-wavelength slots in the input and output regions of layer 3 suppress undesired components of interlayer propagation in those regions. Specific dimensions can be altered somewhat (for example, slot lengths can be made to differ slightly from a quarter wavelength) to suit specific applications, without deviating from the overall design concept.

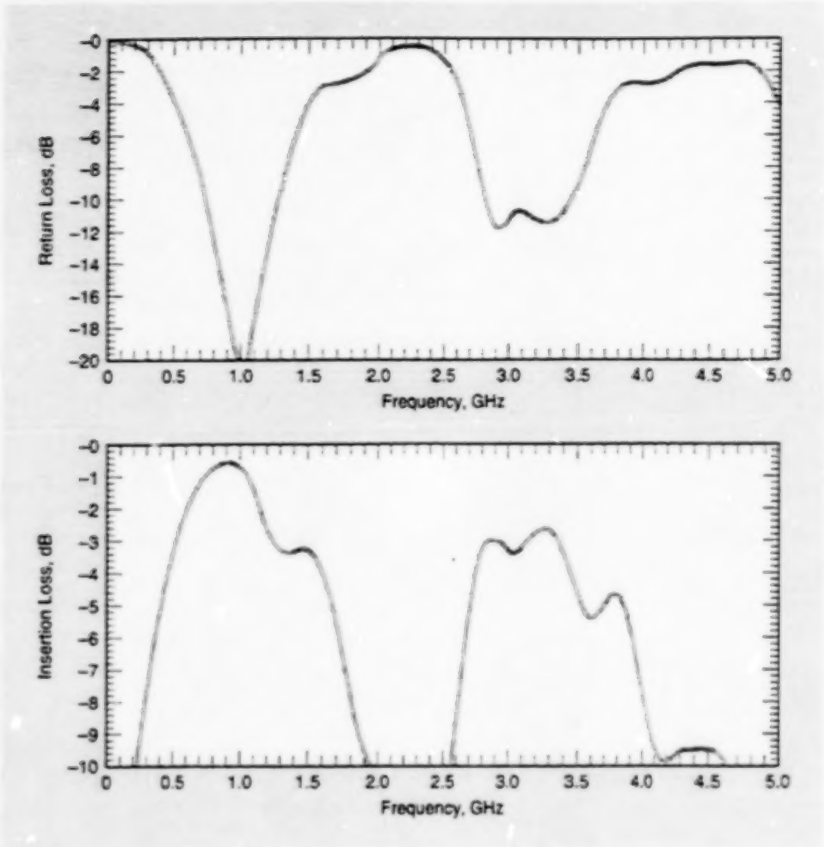

Figure 2. **Return and Insertion Losses** vs. frequency were calculated by a finite-difference time-domain method for the design described in the text.

A trial design for an operating frequency of about 1 GHz specifies the following parameters.

- h = 0.125 in. = 3.175 mm
- w_s = 7 mm
- w_p = 15 mm
- L = 60 mm
- t = 15 mm
- ε_r = 1.1
- Z_{0s} = 61 Ω
- Z_{0p} = 60 Ω

Figure 2 shows return and insertion losses calculated for this design.

This work was done by Ann N. Tulintseff of Caltech for **NASA's Jet Propulsion Laboratory** *Further information is contained in a TSP [see page 1].*

In accordance with Public Law 96-517, the contractor has elected to retain title to this invention. Inquiries concerning rights for its commercial use should be addressed to

Technology Reporting Office
JPL
Mail Stop 122-116
4800 Oak Grove Drive
Pasadena, CA 91109
(818) 354-2240

Refer to NPO-20115, volume and number of this NASA Tech Briefs *issue, and the page number.*

High-Performance HgCdTe Detectors for Remote Sensing: Part 1

A split-geometry design makes it possible to satisfy several special requirements.

Goddard Space Flight Center, Greenbelt, Maryland

Focal-plane arrays of HgCdTe photoconductors have been designed and fabricated to satisfy special requirements for high-performance long-wavelength infrared (LWIR) photodetectors. The special requirements are the following:

- The photoconductive LWIR photodetectors must offer high response and low noise in detection of radiation at wavelengths from 9.1 to 16.6 μm.
- The electrical characteristics of the photoconductive LWIR photodetectors must include high resistance and low power dissipation.
- Each array of the photoconductive LWIR photodetectors must be buttable against another, separately manufactured array of photovoltaic devices on the same focal plane for detecting radiation at wavelengths from 7.1 to 9.1 μm.

The design features a split geometry with all electrical leads on one side of each array; this aspect of the design ensures the required buttability. Furthermore, split-geometry photoconductive detectors inherently have larger current path lengths and resistances than do those of nonsplit geometry; as a result, detector responses are greater and less power is dissipated.

The arrays operate with detectivity of about 3 to 4 × 10^{10} cm $Hz^{1/2}/W$ cutoff wavelength as long as 18 μm. They satisfy all of the special requirements described above. The original application to which the special requirements pertain is to spacecraft instrumentation aboard the CIRS/Cassini spacecraft. There is need for arrays of similar design in other spacecraft; for example, detectors and arrays with similar design are being developed for the Geostationary Operational Environmental Satellite (see the following article). There is also a potential market in terrestrial, scientific, commercial, and military remote-sensing applications.

This work was done by Bob Martineau, Andre Burgess, Sridhar Manthripragada, Frank Peters, Brent Mott, and Peter Shu of **Goddard Space Flight Center**; *Kelley Hu and Jack Shi of HSTX; and Sachidananda Babu of Ball Aerospace. Further information is contained in a TSP [see page 1].*

GSC-13812

High-Performance HgCdTe Detectors for Remote Sensing: Part 2

Sweepout is reduced to improve performance.

Goddard Space Flight Center, Greenbelt, Maryland

The split-geometry design for arrays of photoconductive HgCdTe infrared photodetectors described in the preceding article can also be used to mitigate the deleterious effect of a phenomenon called "sweepout," which degrades performance. Sweepout occurs in conventional small HgCdTe photodetectors operated at high bias voltages; it causes undesired recombination of minority charge carriers at metal/semiconductor interfaces.

The split-geometry design improves performance by delaying the onset of sweepout to higher bias levels. It increases current-path lengths and thereby increases the electrical resistances of detectors. The split-geometry design is being used in the development of improved long-wave-sounder (LWS) detectors for the Geostationary Operational Environmental Satellite (GOES), and is expected to be used in the development of GOES imaging devices.

When detectors of split-geometry design are operated under optimal bias conditions, they exhibit responsivities and detectivities higher, and power dissipations and 1/*f*-noise knees lower, than those of conventional LWS photodetectors. By combining the split-geometry design with operation at relatively low bias, one can minimize the deleterious effect of sweepout. HgCdTe devices designed and operated following this approach have exhibited detectivities as high as 6×10^{10} cm $Hz^{1/2}/W$ at a temperature of 80 K and a cutoff wavelength of 17.2 μm.

This work was done by Bob Martineau, Andre Burgess, Sridhar Manthripragada, Frank Peters, Brent Mott, and Peter Shu of **Goddard Space Flight Center** *and Kelley Hu and Jack Shi of HSTX. Further information is contained in a TSP [see page 1].*

GSC-13810

Improvements in Fabrication of HgCdTe Photodetectors

Two modifications address issues of spectral response and cost of fabrication.

Goddard Space Flight Center, Greenbelt, Maryland

Two improvements have been made to solve two problems that arise in conjunction with a fabrication process in which an HgCdTe photodetector is mounted on an alumina substrate with epoxy. Although most of the HgCdTe-photodetector industry has abandoned this process in favor of epitaxial deposition, epoxy mounting is still used in some special applications.

The first problem is to reduce large variations in detector response as a function of wavelength; that is, to obtain more nearly even spectral response. The sharp variations in the spectral response are associated with resonances caused by interference between reflections from the alumina substrate and the front surface of the detector. The first improvement is to load the epoxy with 0.05-μm alumina grit; this solves the spectral-response problem by suppressing reflections from the substrate.

The second problem arises as follows: During the mounting procedure, the HgCdTe/epoxy/alumina structure is compressed, causing some of the epoxy to flow out and form a ridge around the perimeter of the HgCdTe wafer. The epoxy ridge prevents the use of contact photolithography in subsequent fabrication steps, making it necessary to resort to more expensive and difficult noncontact optical photolithography. The problem is to prevent the formation of the epoxy ridge so that contact photolithography can still be used.

Accordingly, the second improvement is to change the mounting procedure to prevent the formation of the epoxy ridge. In the improved mounting procedure, weight is applied to the HgCdTe/epoxy/alumina structure while the structure is heated. Any excess epoxy squeezed out is removed by use of solvent spray. The epoxy is then cured.

This work was done by Bob Martineau, Andre Burgess, Sridhar Manthripragada, Frank Peters, Brent Mott, and Peter Shu of **Goddard Space Flight Center**; *Kelley Hu and Jack Shi of HSTX; and Sachidananda Babu of Ball Aerospace. Further information is contained in a TSP [see page 1].*

GSC-13811

BLANK PAGE

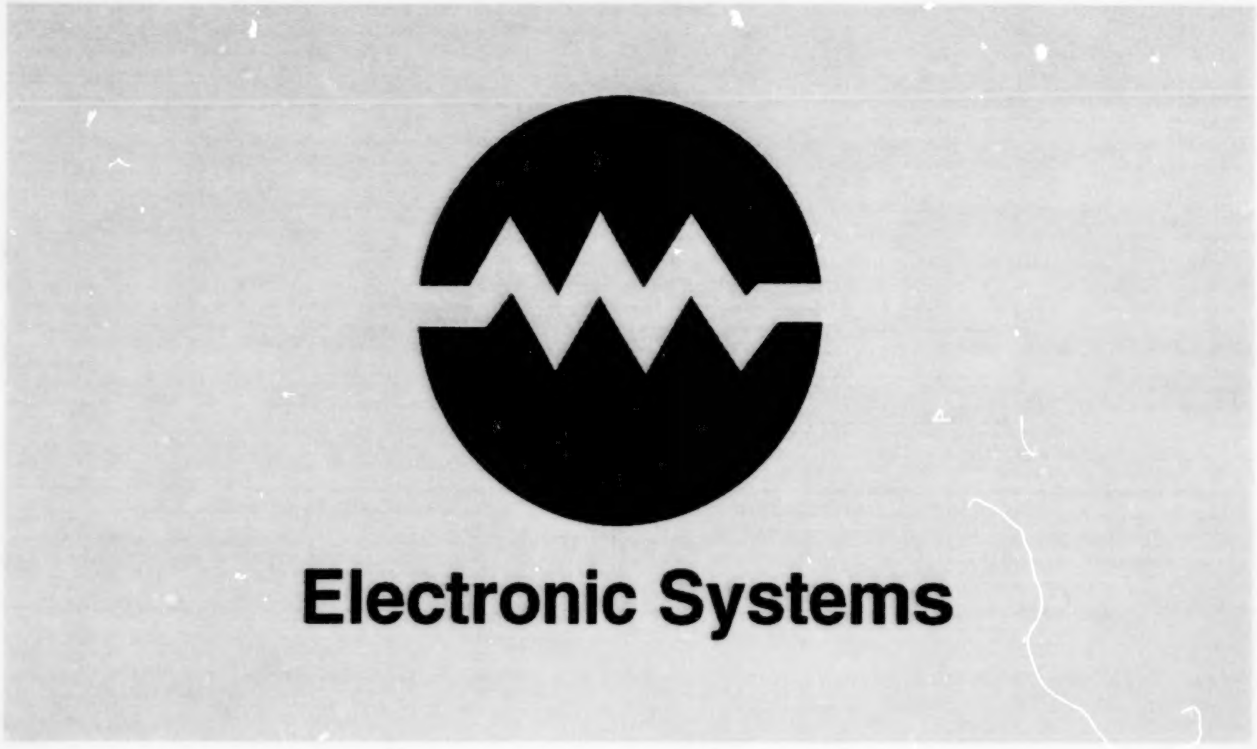

Electronic Systems

Hardware, Techniques, and Processes

17 Software for Operating a Forward-Link-Simulator Card

17 Mobile System for Control of a Remote Rocket-Launching Range

BLANK PAGE

Software for Operating a Forward-Link-Simulator Card

This is the first such software in Digital Unix.

Goddard Space Flight Center, Greenbelt, Maryland

A computer program has been developed to serve as the means for setting up, controlling, and receiving information on the status of a forward-link-simulator card in a Digital Equipment Corporation (DEC) Alpha computer that runs the Digital Unix operating system. The program performs functions of both a device driver and an application-program interface (API).

Some definitions of terms are prerequisite to a meaningful description of this development. "Link" as used here signifies a radio communication link that conveys digital data and command signals between an Earth station and a spacecraft. A forward or a return signal link in this context is an Earth-to-spacecraft or a spacecraft-to-Earth link, respectively. "Card" as used here signifies a printed-circuit board that holds special-purpose electronic circuitry. "Device-driver" as used here signifies software — typically at the lowest level — that communicates directly with the circuitry.

Before this program became available, there was no Digital Unix driver or API software for the forward-link-simulator card. It was necessary to operate the forward-link-simulator card by use of the Digital Unix driver software for another card — the return-link processor card (RLPC) that is functionally different, has a different address map, and has no reading or writing interface. The API software used previously was based on Windows NT API calls, which contain Windows-NT-specific code that does not work in Unix. For transferring data, the Windows NT code does not use direct memory access (DMA) and instead uses slower memory moves. There are no reading- or writing-interface components in either the Windows NT API or the Digital Unix RLPC-driver software used previously.

The present program is written in the C computing language. The driver portion, called "fwlc.mod," performs the system and low-level functions of an interface to the forward-link-simulator card. In the development of the API portion, Windows NT system code was removed and replaced and reading and writing interface code and a DMA transfer capability were added. Called "apiLib.a," the API portion contains function calls that increase the functionality of the card and implements a threaded DMA transfer.

In comparison with the previous RLPC-driver software, the driver component of the present software implements a simpler and more classical approach. As a result, the present software is more portable and application programs that use the driver component can be executed in user mode rather than in kernel (privileged) mode.

This work was done by David Fisher of Stinger Ghaffarian Technology and Robert Kuntz of RMS for **Goddard Space Flight Center**. *Further information is contained in a TSP [see page 1].*
GSC-14035

Mobile System for Control of a Remote Rocket-Launching Range

A single unit replaces multiple units that had to be connected to each other on range.

Goddard Space Flight Center, Greenbelt, Maryland

The Wallops Flight Facility of the Goddard Space Flight Center has designed and built in-house a Mobile Range Control System (MRCS), which is a self-contained system to be deployed in support of rocket launches at remote ranges in cases in which termination of flight may be required for safety purposes. The MRCS includes data-acquisition subsystems, real-time data-computation subsystems, range-safety displays, command/destruct transmitters, and supporting communication subsystems, all together providing for remote range control.

Prior to the development of the MRCS, subsystems in several mobile containers were integrated on range to satisfy requirements to provide functions similar to those now performed by the MRCS. In comparison with the older collection of subsystems in separate containers, the fully integrated MRCS can be tested more completely prior to shipment, and it reduces mission-support time and cost. Improvements incorporated into the MRCS include state-of-the-art hardware and real-time software data processing which generates and displays range safety real-time instantaneous impact prediction data derived from mobile radar and telemetry tracking systems. The MRCS provides safe and reliable conduct of Expendable Launch Vehicles (ELVs) and an environment that is comfortable for operators.

This work was done by H. Dean Price of **Goddard Space Flight Center**. *Further information is contained in a TSP [see page 1].*
GSC-14021

BLANK PAGE

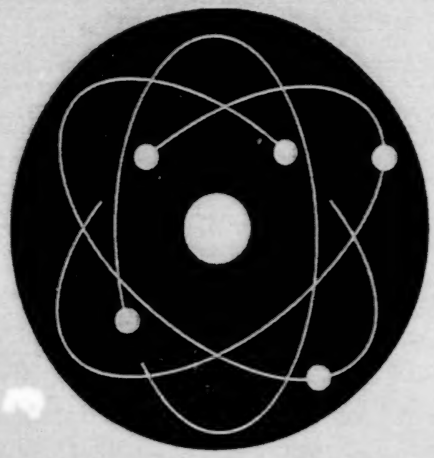

Physical Sciences

Hardware, Techniques, and Processes

21 Programmable Multizone Directional-Solidification Furnaces
22 Scanning Surface-Plasmon Filters for Miniature Spectrometers
23 Thermal Batteries Made With Nanostructured Material
24 Miniature Lambda Sensors for Engine-Control Systems
25 Sensor for Monitoring Concentration of Methanol in Water
26 Segmented-Aperture Michelson Interferometer
26 Foam Heat Exchangers

Books and Reports

27 Details of Apparatus for Advanced Ultrasonic C-Scan Imaging

BLANK PAGE

Programmable Multizone Directional-Solidification Furnaces

These furnaces would afford improved capabilities for shaping and translation of thermal gradients.

Marshall Space Flight Center, Alabama

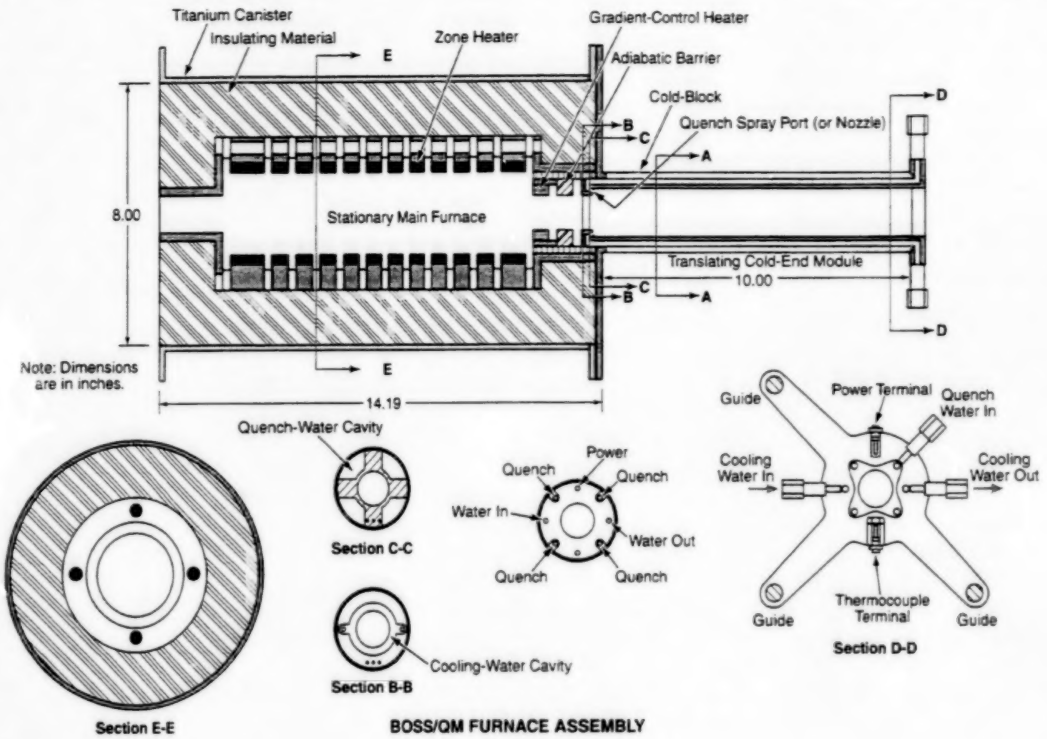

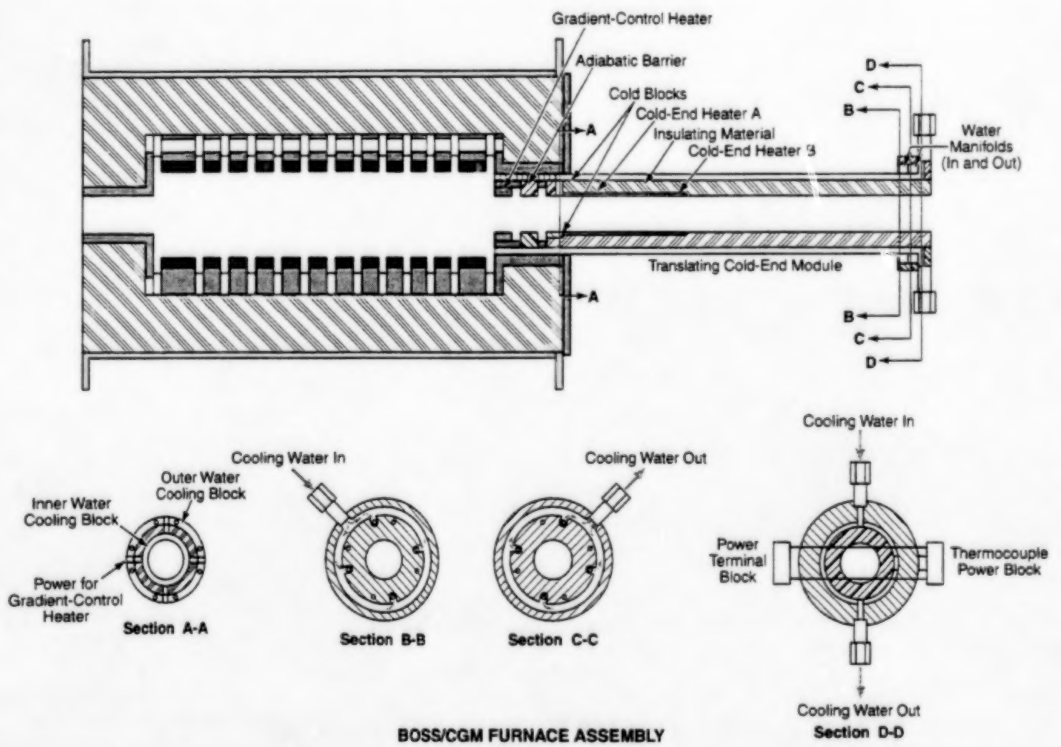

Two **BOSS Furnace Assemblies** are shown in simplified form to illustrate the arrangement of major components. For the sake of clarity, outer containers and drive mechanisms for translating the cold-end modules are omitted from these drawings.

Programmable multizone furnaces with enhanced designs have been proposed for use in processing materials by directional solidification or, optionally, by related techniques of float-zone or isothermal solidification. Like some other directional-solidification furnaces reported previously in *NASA Tech Briefs* and elsewhere, these furnaces would incorporate multiple, individually controllable electric heaters stacked at a succession of axial locations in a stationary cylindrical main canister for generating, shaping, and translating specified axial temperature profiles (specified temperatures and/or temperature gradients) under electrical control. These furnaces would also incorporate cold-end modules that could be translated axially and telescoped into the main canisters to provide additional versatility for control of cold-end temperature profiles.

Because it would afford options for a combination of mechanical (translational) and electrical control of temperature profiles, a furnace of this type would be called a "bi-operational solidification system" (BOSS) to distinguish it from older multizone furnaces that feature electrical or translational (but not both) modes of temperature-profile control. The BOSS concept offers opportunities for achieving (1) compact furnace design, (2) increased versatility for programming a variety of stationary and moving temperature profiles, and (3) high thermal efficiencies through reduced (relative to other directional-solidification furnaces) heat losses, with total power-consumption levels comparable to those of translation (only)-type directional-solidification furnaces.

A typical BOSS (see figure) would include 12 zone heaters separated by spacers that would reduce heat conduction between zones and thereby also enhance thermal control of each zone. The axial lengths of the end heaters would be made greater than those of the other heaters to provide additional heat capacity to overcome heat losses from the ends. Each heater would comprise an electrically resistive wire wound in a groove on the radially outermost edge of a washerlike disk of thermally insulating material. (Consequently, each heater would act as an insulator when not powered.) Thermocouples for measuring temperatures in the heater zones would be included. Power and thermocouple leads could be routed axially or radially through a layer of insulating material that would surround the heaters.

The cold-end module could be of either of two types: (1) a quench module (QM) or (2) a crystal-growth module (CGM). A QM would include a water-cooled cold block (or quench block), a quench-spray port or nozzle at the entrance to the cold block, and a gradient-control heater separated from the cold block by an adiabatic barrier. In conjunction with the zone heaters in the stationary main canister, a QM would provide a controllable, translatable temperature gradient.

A CGM would also include a gradient-control heater and an adiabatic barrier, but would differ from a QM in that the quench capability would be replaced by a cold-end temperature-control capability. Instead of a single cold block, there would be two cold blocks, which could be actively cooled by water or operate in a passive (uncooled) mode. Two cold-end heaters mounted on a common mandrel would provide a capability for finer control of the cold-end temperature profile.

This work was done by Jack E. Robertson of Al Signal Research, Inc., for **Marshall Space Flight Center**. *Further information is contained in a TSP [see page 1].*
MFS-26524

Scanning Surface-Plasmon Filters for Miniature Spectrometers

Sizes and masses of spectrometers could be reduced greatly.

NASA's Jet Propulsion Laboratory, Pasadena, California

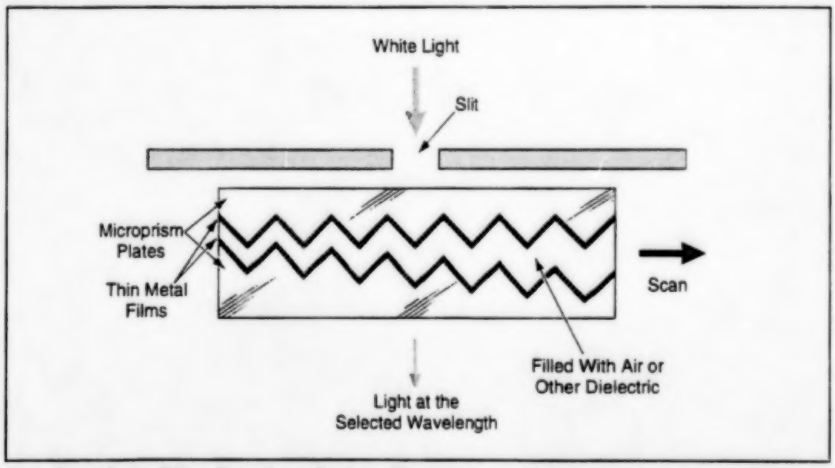

This **Band-Pass Filter Based on Surface Plasmons** would feature a tapered gap between microprism plates. A scanning mechanism would be used to translate the microprism plates sideways to select the desired gap thickness and thus the desired wavelength of peak transmission.

Scanning filters based on surface plasmons would be used as the adjustable wavelength-selective (band-pass) devices in a class of proposed miniature spectrometers. These filters would occupy much less space and weigh much less than do the diffraction gratings and other wavelength-selective optics of conventional spectrometers; as a result, the proposed spectrometers would be correspondingly smaller and less massive.

In a recently developed tunable band-pass filter based on surface plasmons, the pass wavelength band is adjusted by changing the airgap between two prisms. The filters in the proposed spectrometers would implement an alternative approach to tuning. A filter of this type would include two glass plates separated by a narrow gap filled with air or another dielectric with a low index of refraction. The facing surfaces of the plates would be grooved to form microprisms and coated with thin metal films. In a typical example, the dielectric would be air and the microprisms would be made of BK-7 (or equivalent) glass, formed for an angle of incidence of 41.5°, and coated with silver to a thickness of 40 nm.

The microprism plates would be tilted slightly to make the gap thickness vary from one edge to the other. The assembly of plates would be mounted on a scanning mechanism below a spectrometer slit, so that by use of the mechanism, the thick-

ness of the gap illuminated through the slit could be varied. Inasmuch as the wavelength of peak transmission would depend on the thickness of the gap, scanning by use of the mechanism would thus result in variation of the pass wavelength band. In the example cited above, scanning from a gap 300 nm thick to a gap 5,000 nm thick would shift the wavelength of peak transmission from 400 to 1,600 nm.

This work was done by Yu Wang and Bedabrata Pain of Caltech for **NASA's Jet Propulsion Laboratory**. *Further information is contained in a TSP [see page 1].*
NPO-20179

Thermal Batteries Made With Nanostructured Material

Power densities can be increased by use of finer-grained cathode powder.

Lewis Research Center, Cleveland, Ohio

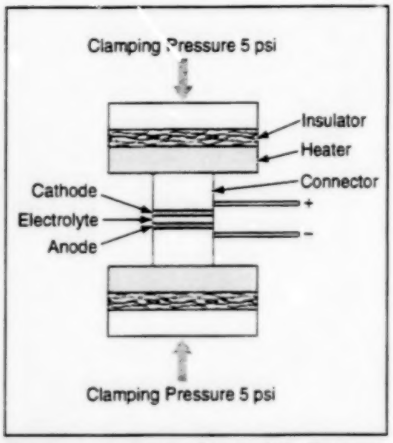

Figure 1. A **Basic Single-Cell Thermal Battery** contains electrode and electrolyte disks. Unlike power cells used in many commercial products, this cell must be activated by heating to melt the electrolyte.

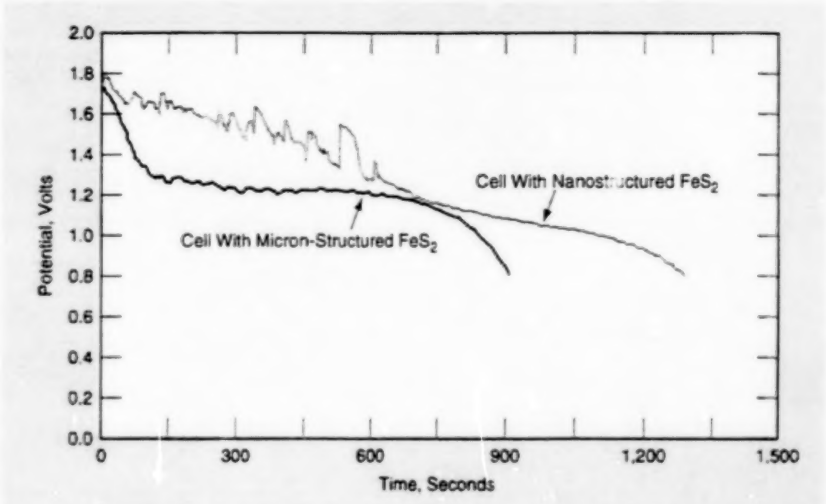

Figure 2. **Voltages Generated by Cells** of the types described in the text were measured during constant-current (0.4 A) discharges at a temperature of 400 °C.

Early experiments in a continuing research program have demonstrated that thermal batteries made from powdered solid electrode and electrolyte materials can be improved by use of smaller (nanometer vs. micrometer size) cathode powder grains. The improvements include the possibility of fabricating and using thinner cathodes, plus increases in mechanical robustness, thermal stability, and overall power density.

A thermal battery is a primary battery that is activated by heating to melt the solid electrolyte to supply electrical power for a limited time. Thermal batteries are highly reliable energy sources with high power densities and long shelf lives. They are particularly useful for supplying short-term power in expendable weapons (e.g., torpedoes and projectiles) and exploratory spacecraft; likely future commercial applications could include generating emergency power in aircraft and providing startup power for automobiles with weak batteries.

A single-cell thermal battery of the type under study in this research program (see Figure 1) contains an electrolyte disk stacked between an anode and a cathode disk. Each disk is made by cold-pressing the appropriate cathode, electrolyte, or anode powder. Heretofore, thermal batteries have been manufactured by techniques that impose lower limits on disk thicknesses needed to ensure adequate mechanical strengths. Accordingly, achievable power densities and other performance characteristics have been limited, and progress toward miniaturization and toward enhancement of activation characteristics and of safety has been impeded.

The anode material used in the experiments was an alloy of 44 percent Li + 56 percent Si, supplied as a powder of micron-scale particles. The anode disks were formed by pressing this powder in a 2-cm-diameter round steel die at 6,000 psi (41 MPa). The electrolyte material included a powder of eutectic salt comprising 45 percent LiCl + 55 percent KCl. To strengthen the electrolyte disks, the eutectic salt powder was blended with 35 percent of MgO powder. The blended powder was pressed at 4,000 psi (28 MPa) to form electrolyte disks.

The cathodes were made from a blend of 68 percent FeS_2 powder, 30 percent of the eutectic salt powder, and 2 percent of SiO_2. The blend was pressed into disks at 4,000 psi (28 MPa). To provide a basis for comparison, the FeS_2 powder used to make some cathode disks had particle sizes of the order of 1 μm, while that used to make the other cathode disks had an average particle size ≈25 nm. The nanostructured FeS_2 powder was made by ball-milling the micron FeS_2 powder.

For equal weights of blended powder and identical pressing conditions, the cathode disks made from nanostructured FeS_2 came out 23 percent thinner and thus 30 percent denser than the cathode disks made from micron-scale FeS_2. The nanostructured disks were found to be more robust than the others by comparison of degrees of shattering in a simple drop test. Thus, it was demonstrated that thinner, more robust cathode disks can be made by use of nanostructured instead of micron-scale FeS_2 powder.

In thermogravimetric tests of the thermal decomposition of FeS_2 into FeS + S, the nanostructured-FeS_2 cathodes were found to be more stable. Finally, the discharge electrical performances of batteries containing nanostructured-FeS_2 cathodes were found to be superior to those con-

taining micron-scale-FeS_2 cathodes (see Figure 2): The discharged electrical energy per unit mass averaged over all the cell material (electrodes + electrolyte) was found to be 109 J/g in the nanoscale case and 58 J/g in the micron-scale case.

This work was done by Ming Au, Yabin Lei, and Tapesh Yadav of Nanomaterials Research Corp. for **Lewis Research Center**.

Inquiries concerning rights for the commercial use of this invention should be addressed to NASA Lewis Research Center, Commercial Technology Office, Attn: Steve Fedor, Mail Stop 4–8, 21000 Brookpark Road, Cleveland, Ohio 44135. Refer to LEW-16698.

Miniature Lambda Sensors for Engine-Control Systems

The feasibility of sensors made from a nanoceramic has been demonstrated.

Lewis Research Center, Cleveland, Ohio

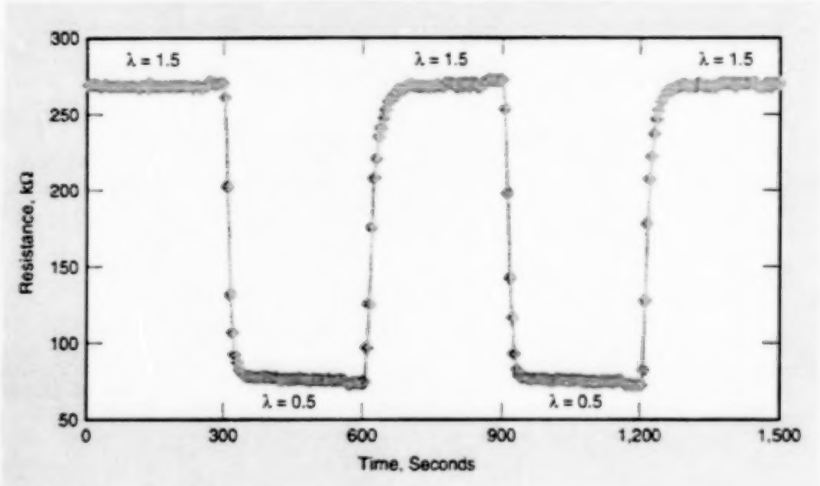

The **Electrical Resistance of a Pellet of Ga_2O_3 Nanoceramic** was measured in a flowing mixture of CO, O_2, and N_2 as the composition of the mixture was alternated between $\lambda = 0.5$ and $\lambda = 1.5$.

Small, lightweight sensors that exploit the unique characteristics of nanoceramics are being developed for use in measuring air/fuel ratios in the exhaust gas flows of advanced aircraft engines. Adaptive control systems would process the readings from these sensors, along with other sensory and control inputs, to generate engine commands to maximize fuel efficiency and minimize emissions of undesired exhaust products. Sensors and control systems of this type could also be used to enhance the operation of automotive and other internal-combustion engines that burn a variety of fuels, and of stationary combustors like furnaces and kilns.

The developmental sensors are called "lambda sensors" because the fuel/air ratio of particular relevance in this context is denoted by the symbol λ (lambda). The defining equation is $\lambda \equiv$ [actual value of (density of oxygen/density of fuel)]÷[stoichiometric value of (density of oxygen/density of fuel)]. Ordinarily, a monitoring and control system would be designed to keep λ as close as possible to 1. Heretofore, commercially available sensors have not offered the rapid response and high sensitivity needed for monitoring and controlling λ when λ varies from substoichiometry (0.5) to super-stoichiometry (1.5).

Nanomaterials and, in particular, nanoceramics, are novel high-precision materials that are synthesized with selected crystalline sizes <100 nm. The microstructure of a typical nanomaterial is such that there is a very large concentration of grain boundaries, and between 20 and 60 percent of the atoms are interfacial. The large interfacial area is conducive to rapid equilibration and rapid diffusion, both of which are essential for rapid and reliable sensor operation.

Equally important, the complex of electrical and chemical interactions at the interfaces and within the bulk crystalline material can be exploited for sensing chemical species of interest. The net effect of these interactions is that the electrical resistance of a piece of nanoceramic exposed to pure air or oxygen differs from its electrical resistance during exposure to air or oxygen with a fuel or other analyte gas mixed in, and the ratio between the two resistances can be taken as a measure of the concentration of the analyte in the gas mixture. A major portion of the present effort to develop λ sensors is devoted to optimizing crystalline structures, mostly by tailoring grain sizes, in order to exploit combinations of bulk and surface effects to obtain rapid response and high sensitivity.

Initial experiments have been performed on λ sensors made from nanoscale Ga_2O_3 powders that were synthesized by a solvent-precipitation technique and by a thermal-quench technique. Fabrication of each sensor began with squeezing of Ga_2O_3 powder at a pressure of 2,000 psi (14 MPa) to form a pellet. The pellets were sintered for one hour in air at a temperature of 1,300 °C. By use of silver paste as a bonding agent, the pellets were bonded to an alumina substrate with platinum electrodes for measuring the electrical resistance of the pellets.

The figure is a plot of data from an experiment in which a sensor was exposed to a synthetic exhaust mixture of CO (regarded as the fuel gas), O_2, and N_2. In this experiment, λ was made to alternate between 0.5 and 1.5. The plot indicates the feasibility of λ sensors made from Ga_2O_3 nanoceramics, though the response time is still longer than the maximum (about 10 ms) allowable in engine-control applications. Refinements in the sensor materials and designs will be necessary to reduce response times. Further research will also be needed to ensure stability and reproducibility of sensor characteristics, to increase durability, to enhance sensitivity, to achieve further miniaturization, and to establish temperatures and develop temperature controls for reliable sensor operation.

This work was done by Chuanjing Xu and Tapesh Yadav of Nanomaterials Research Corp. for **Lewis Research Center**. *No further documentation is available.*

Inquiries concerning rights for the commercial use of this invention should be addressed to NASA Lewis Research Center, Commercial Technology Office, Attn: Steve Fedor, Mail Stop 4–8, 21000 Brookpark Road, Cleveland, Ohio 44135. Refer to LEW-16700.

Sensor for Monitoring Concentration of Methanol in Water

Speed of response and dynamic range exceed those of other methanol sensors.

NASA's Jet Propulsion Laboratory, Pasadena, California

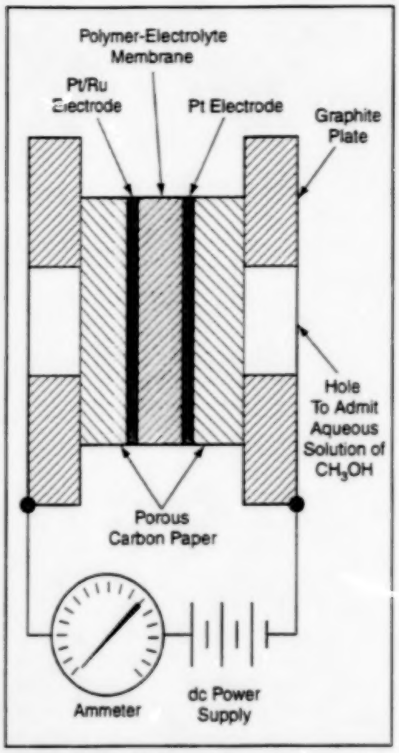

Figure 1. This **Methanol Sensor** is based on electrochemical oxidation of methanol coupled with electrochemical reduction of water.

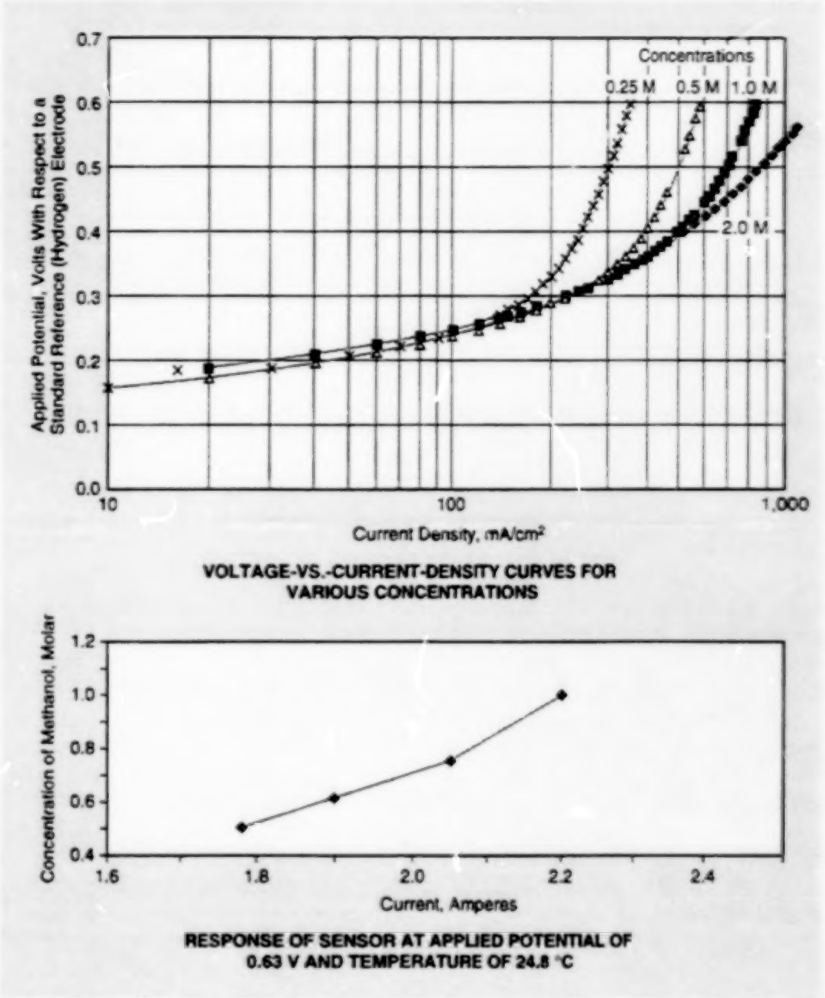
Applied Potential, Volts With Respect to a Standard Reference (Hydrogen) Electrode
Concentrations
0.25 M
0.5 M
1.0 M
2.0 M
Current Density, mA/cm²
VOLTAGE-VS.-CURRENT-DENSITY CURVES FOR VARIOUS CONCENTRATIONS
Concentration of Methanol, Molar
Current, Amperes
RESPONSE OF SENSOR AT APPLIED POTENTIAL OF 0.63 V AND TEMPERATURE OF 24.8 °C

Figure 2. The **Electric Current in the Sensor** increases with the applied potential and with the concentration of methanol in water. The current also depends on temperature. For a specified temperature and applied potential, the current thus serves an indication of the concentration of methanol.

A robust sensor based on the electrochemical oxidation of methanol has been developed for use in measuring the concentration of methanol dissolved in water. The sensor is expected to be particularly useful in continuous monitoring and control of the concentration of an aqueous solution of methanol metered into a liquid-feed, direct-oxidation methanol fuel cell.

Other methanol sensors respond to changes in concentration too slowly to be useful for monitoring and control. Moreover, methanol sensors based on spectroscopy are relatively insensitive at high concentrations. The present sensor responds rapidly enough for monitoring and control. It also offers wide dynamic range; it can measure concentrations from 0.01 M to 5 M. Furthermore, it functions over the entire temperature range of liquid water at normal atmospheric pressure; that is, from 0 to 100 °C.

The sensor (see Figure 1) resembles a small liquid-feed, direct-oxidation fuel cell in some respects, but is operated in a different manner. It includes a polymer-electrolyte membrane coated on one side with a catalytic electrode composed of Pt/Ru-alloy powder and coated on the other side with a catalytic electrode composed of Pt black. Some details of the preparation of the Pt/Ru powder, the polymer-electrolyte membrane, and coating the membrane with the Pt/Ru powder were described in "Making Catalysts and Electrodes for Liquid-Feed Fuel Cells" (NPO-19893) *NASA Tech Briefs*, Vol. 20, No. 10 (October 1996), page 60. The coated membrane is pressed between sheets of the porous carbon paper. The resulting sandwich is mounted between graphite plates that act as both current collectors and structural supports. Circular openings in the graphite plates expose the sandwich to the aqueous solution of methanol.

When the Pt/Ru and Pt electrodes are connected to the positive and negative sides, respectively, of a dc power supply, electric current flows through the sensor, causing the following reactions:

$$CH_3OH + H_2O \rightarrow CO_2 + 6H^+ + 6e^-$$

at the Pt/Ru electrode and

$$6H^+ + 6e^- \rightarrow 3H_2$$

at the Pt electrode.

As the applied potential increases, the rate of this reaction (and thus the electric current) becomes subject to limitation on the rate of transport of methanol to the surface of the Pt/Ru electrode. As the concentration of methanol increases, more methanol becomes available for transport, making it possible to sustain a larger trans-

port-limited current. Thus, for a given applied potential, the current increases with the concentration of methanol (see Figure 2). This behavior is exploited in designing the methanol sensor; in the basic mode of operation, one applies a specified potential in the range in which current is strongly transport-limited (e.g. 0.63 V) and measures the current as an indication of the concentration of methanol.

The response of the sensor also depends on temperature. At each operating temperature of interest, the sensor is calibrated by applying the potential and measuring the current in the presence of aqueous solutions with known concentrations of methanol.

This work was done by Sekharipuram Narayanan, William Chun, and Thomas Valdez of Caltech for **NASA's Jet Propulsion Laboratory**. *Further information is contained in a TSP [see page 1].*

In accordance with Public Law 96-517, the contractor has elected to retain title to this invention. Inquiries concerning rights for its commercial use should be addressed to

Technology Reporting Office
JPL
Mail Stop 122-116
4800 Oak Grove Drive
Pasadena, CA 91109
(818) 354-2240

Refer to NPO-20125, volume and number of this NASA Tech Briefs *issue, and the page number.*

Segmented-Aperture Michelson Interferometer

Size and weight could be reduced.

NASA's Jet Propulsion Laboratory, Pasadena, California

In a proposed modification of the basic design of a Michelson interferometer, the beam aperture would be split into a number ($N \geq 2$) of smaller areas and the optics arranged so that the beam in each area would generate a distinct segment of the overall desired interferogram. Each segment of the interferogram would correspond to a different segment of the overall optical-path difference (OPD) needed to obtain the desired spectral resolution. As explained below, the advantage of the proposed modification is that the size and mass of a Michelson interferometer could be reduced considerably.

In a traditional Michelson interferometer, it is necessary to move one mirror a distance $x/2$ to obtain an OPD of x. If the beam is split into N smaller beams, each generating a different part of the interferogram, then the same overall OPD is obtained by moving the mirror a much smaller distance — only $x/2N$. The moving-mirror arm is a major contributor to the volume, mass, and mechanical complexity of a Michelson interferometer; reducing the overall required mirror travel would make it possible to use smaller, simpler mirror-support structures and mirror-translation mechanisms.

According to tradition, the design of an interferometer must provide for a single beam area, wherein the beam is modulated by a single set of interferometer mirrors. Traditional thinking on this subject has been dominated by the assumption that continuity of the interferogram must be maintained. The proposed modification would violate the traditional requirement of continuity. The violation is justified by the realization that the requirement of continuity is not based on fundamental physics; provided that one can find a way to splice the segments together seamlessly into one interferogram, there is no physical reason to refrain from use of a segmented aperture.

The N segments of an interferogram would be collected in one mirror stroke and would be digitized. The requirement for seamless splicing of the segments translates to a requirement to sample all of the segments on the same computational grid and to match their amplitudes. For this purpose, it would likely be necessary to oversample each segment on its own grid, then digitally resample it to place it on the same grid as that of the adjacent segment. The segments would be adjusted accordingly by comparing small regions of overlap between them and compensating for differences in sampling, signal amplitude, and offset. After adjustment, the segments could be spliced together to form the full interferogram, which could then be Fourier-transformed in the normal way.

Of course, segmentation of the interferometer would entail some engineering compromises. The decrease in overall size, mass, and mechanical complexity would be partly counteracted by a corresponding increase in the number of photodetectors and associated signal-processing circuits, by the need to prevent optical cross-talk between segments, and by an increase in the complexity of computations needed to process the signal-chain outputs. Fortunately, most of these considerations could be addressed by use of modern electronic signal-processing and computing equipment. Recent advances in electronics have yielded great increases in performance and decreases in size and power consumption.

This work was done by Michael Eastwood and Crofton Farmer of Caltech for **NASA's Jet Propulsion Laboratory**. *Further information is contained in a TSP [see page 1].*

NPO-20346

Foam Heat Exchangers

Heat exchangers and pumps can be made smaller, lighter, and less expensive.

Lewis Research Center, Cleveland, Ohio

Experiments have demonstrated the feasibility of heat exchangers with flow channels containing open-cell metallic foams. Nonmetallic foams could also be used. One proposed design calls for an open-cell foam in the annular region between an inner and an outer tube, with a heat-transfer fluid flowing along the annular region while either the outer or the inner tube is heated by flowing hot gas. Heat would be transferred from the heated tube wall to the fluid with an efficiency greater than that of a simple tube heat exchanger. The increase in heat-transfer efficiency would result from the large surface area of the foam in contact with the cooling fluid and from turbulence induced by the ligaments of the foam in the flow path. Thermal conduction between the

wall and the foam would also make a small contribution.

Greater heat-transfer efficiency should make it possible to design smaller, lighter heat exchangers for some applications. Another advantage of foam heat exchangers is that all flow paths through foam are interconnected, so that if a flow becomes obstructed by debris lodged in foam at one place in a channel, the flow can continue elsewhere in the channel; in other words, complete blockage of a channel is unlikely. This is in contrast to the situation in a heat exchanger containing narrow brazed tubes and/or narrow, precisely machined channels, which can become blocked more readily. Moreover, in comparison with machined-channel and brazed-tube heat exchangers, foam heat exchangers can be fabricated more easily and at lower cost.

Remarkably, a properly designed foam heat exchanger exhibits less back pressure than does a machined-channel or brazed-tube heat exchanger of equal heat-transfer capacity. Thus, a smaller pump can be used to circulate the heat-transfer fluid.

This work was done by Arthur J. Fortini and Robert H. Tuffias of Ultramet for **Lewis Research Center**. *Further information is contained in a TSP [see page 1].*

Inquiries concerning rights for the commercial use of this invention should be addressed to NASA Lewis Research Center, Commercial Technology Office, Attn: Steve Fedor, Mail Stop 4–8, 21000 Brookpark Road, Cleveland, Ohio 44135. Refer to LEW-16579.

Books and Reports

Details of Apparatus for Advanced Ultrasonic C-Scan Imaging

A report comprising the main contents of U. S. Patent 5,750,895 presents detailed information on the subject of "Apparatus for Advanced Ultrasonic C-Scan Imaging (GSC-13524), *NASA Tech Briefs*, Vol. 21, No. 4 (April 1997), page 34. The apparatus is a computer-controlled ultrasonic C-scan instrumentation system that includes an ultrasonic transducer, an electronic pulser/receiver, a dual timing gate, a peak detector, and a timer. The transducer is scanned in a horizontal (*x,y*) plane parallel to the top surface of a specimen. At each position *x,y*, the computer estimates the depth of any defect or other feature that reflects ultrasound, using the speed of sound and the measured round-trip travel time of the ultrasonic signal between the top surface of the specimen and the feature. The time gate of the peak detector is chosen so that the peak-detector output indicates the amplitude of the reflection from the feature. The computer processes the *x,y* position data and the associated depth and amplitude data into a single three-dimensional-appearing plot of both depth and amplitude as functions of *x* and *y*. The vertical (*z*) axis in the plot represents depth, and a gray scale or color scale indicates amplitude.

This work was done by Engmin James Chem and David W. Butler of **Goddard Space Flight Center**. *To obtain a copy of the report, "Method and Apparatus for Dual Amplitude Time-of-Flight Ultrasonic Imaging," see TSP's [page 1].*

This invention is owned by NASA, and a patent application has been filed. Inquiries concerning nonexclusive or exclusive license for its commercial development should be addressed to the Patent Counsel, Goddard Space Flight Center [see page 1]. Refer to GSC-13524-2.

BLANK PAGE

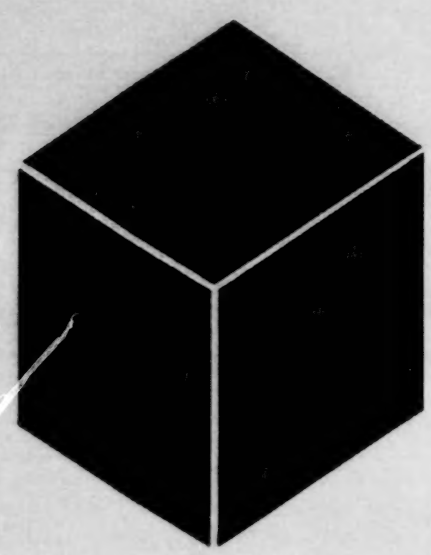

Materials

Hardware, Techniques, and Processes

31 Improved Fabrication of Electrodes for Methanol Fuel Cells
32 Another Improved Method for Making Fuel-Cell Electrodes
33 Electric-Arc and Electrochemical Texturing of Surfaces
34 Lead Bromide Crystals Doped With Silver Bromide
34 Thermal and Mechanical Effects in Graded Composite Cylinders
35 Improved Electrical Connections for Thin-Film Thermocouples

BLANK PAGE

Improved Fabrication of Electrodes for Methanol Fuel Cells

Expensive catalytic metals are utilized more efficiently.

NASA's Jet Propulsion Laboratory, Pasadena, California

A method of fabricating membrane electrode structures for methanol fuel cells involves, among other things, the use of improved sprayers to deposit inks containing catalytic metals on membranes of Nafion™ (or equivalent) perfluorosulfonic acid-based hydrophilic, proton-conducting ion-exchange polymer. In comparison with older methods, the present method provides for faster production with more efficient utilization of the expensive catalytic metals. The present method is thus better suited to mass production.

The older methods do not provide for deposition of uniformly thin catalytic layers on membranes, nor do they afford the flexibility of depositing well-defined multiple thin catalytic layers of different compositions. The present method does provide these capabilities, thus making it possible to tailor catalytic layers more precisely to achieve comparable cell performances with reduced catalyst loadings. The improved sprayers used in the present method contribute to the attainment of these objectives in that they produce slow, fine sprays that can be aimed more precisely on the surface areas to be coated, without wasting sprays on adjacent areas. Moreover, whereas the sprayers used in the older methods frequently became clogged, the improved sprayers are designed to prevent clogging.

The catalytic ink usually comprises the catalytic metal (Pt for the cathode or a mixture of Pt and Ru for the anode), a Nafion™ (or equivalent) ionomer solution, water, and isopropanol, with perhaps a small amount of a polytetrafluoroethylene-based additive. The ingredients of the ink are mixed well by use of ultrasound, and the viscosity of the ink is adjusted, by addition of small amounts of water and isopropanol, to enhance sprayability. The ink is then transferred to the sprayer.

In fabricating a membrane electrode according to the present method, the membrane is first conditioned in water, then soaked in an aqueous solution of isopropanol or methanol; this soaking is necessary to swell the membrane to prevent wrinkling that would otherwise occur when the sprayed catalytic ink subsequently comes into contact with the membrane. The membrane is then mounted in a frame (see figure), which must be nonmetallic to prevent corrosion. Then before the membrane dries out, it is sprayed on one side with catalytic ink. The position and settings of the spray head and the rate of flow of compressed air that drives the sprayer are adjusted to regulate the characteristics of the spray to ensure that the spray does not dry out on its way to the membrane and so that the deposited material bonds to the membrane and forms an electrochemically active surface. The spray-coated membrane is then dried with air at ambient temperature or, optionally, air heated to a temperature between 40 and 60 °C to accelerate drying.

Additional coats of catalytic ink on the same side or on opposite sides can be applied by repeating the spraying and drying steps. Preferably, the layers are applied alternately on the anode and cathode sides to minimize any stresses remaining after the coating process. The areal mass density of a single coat can be as small as 0.1 mg/cm².

Upon completion of coating, the membrane is released from the frame and hot-pressed between anode- and cathode-side carbon-paper supports. The resulting sandwich electrode structure is then stored in water until use.

In experiments, the performances of fuel cells containing electrode structures made by the present method were found to be comparable to those of fuel cells containing electrode structures made by older methods. However, the amounts of catalysts used in the present method ranged from 1 to 2 mg/cm², whereas the amounts used in the older methods were typically about 4 mg/cm². The achievement of comparable performance with less catalytic material by use of techniques suitable for mass production is a significant step toward commercialization and lowering the costs of producing fuel cells.

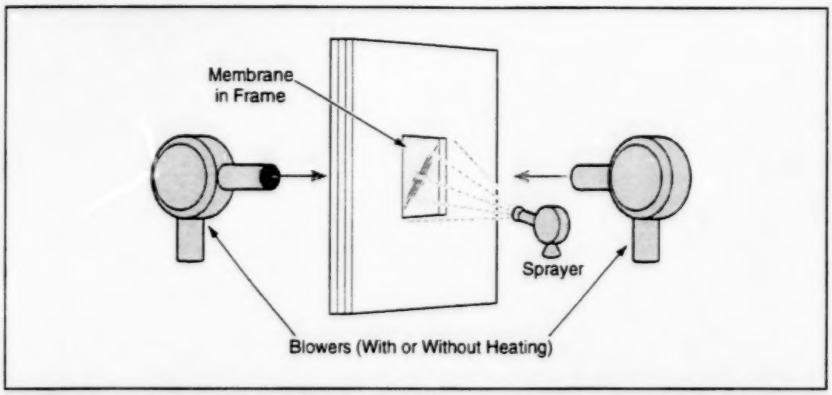

The **Membrane Is Sprayed and Dried** in the frame, which helps to maintain its dimensions and shape. Spraying and drying conditions are adjusted to obtain an adherent deposit of catalytic material, without cracking of the deposit or excessive residual stress in the membrane.

This work was done by William Chun, Sekharipuram Narayanan, Barbara Jeffries-Nakamura, Thomas I. Valdez, and Juergen Linke of Caltech for **NASA's Jet Propulsion Laboratory**. *Further information is contained in a TSP [see page 1].*

In accordance with Public Law 96-517, the contractor has elected to retain title to this invention. Inquiries concerning rights for its commercial use should be addressed to

Technology Reporting Office
JPL
Mail Stop 122-116
4800 Oak Grove Drive
Pasadena, CA 91109
(818) 354-2240

Refer to NPO-19941, volume and number of this NASA Tech Briefs *issue, and the page number.*

Another Improved Method for Making Fuel-Cell Electrodes

Power densities can be increased at low catalyst loadings.

NASA's Jet Propulsion Laboratory, Pasadena, California

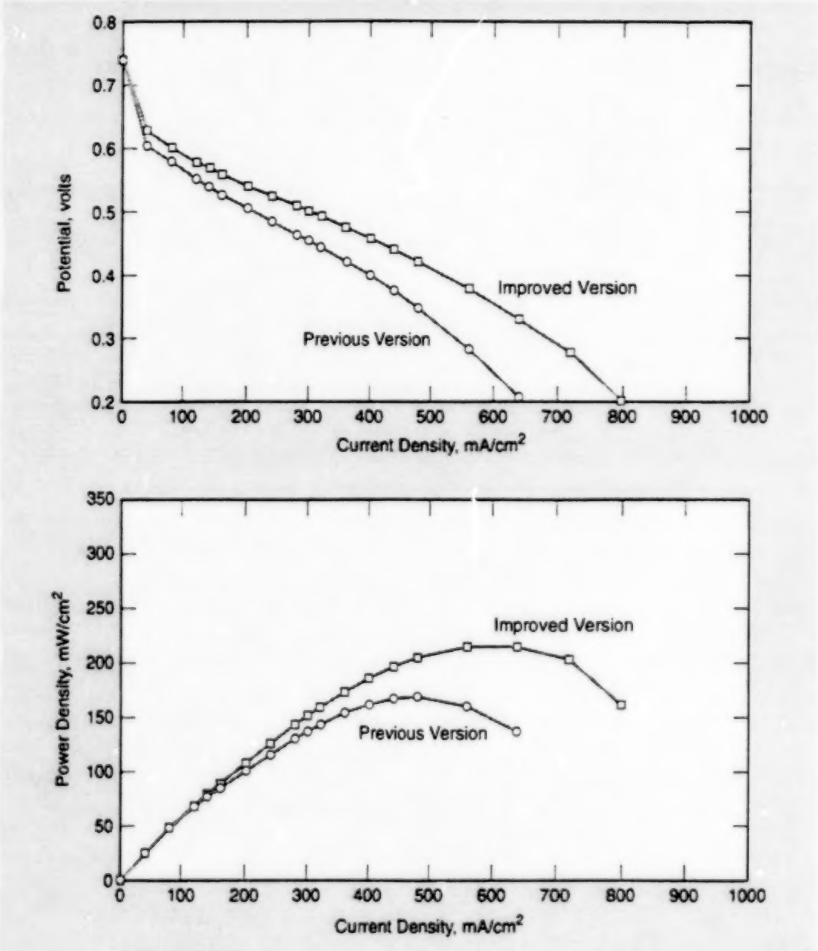

In Terms of Both Voltage and Power Density vs. current density, an electrode structure made by the present method performed better than did one made by a previous method.

An improved method of fabricating membrane electrode structures for methanol fuel cells is similar to the method described in the preceding article, except that in this method, the catalytic ink is poured and spread onto the membrane instead of sprayed. The development of both improved methods was prompted by a need to utilize expensive catalytic material more efficiently.

Older methods of fabricating such electrode structures involve the deposition of catalysts on porous carbon paper substrates, which are then hot-pressed onto solid-electrolyte membranes. In a typical case, at least half the catalyst becomes immobilized deep within the pores of the substrate. This portion of the catalyst is not accessible for electrochemical reactions, and is not available for the formation of the desired large-area, electrochemically active interface between the catalyst-coated substrate and the membrane.

Both improved processes include pretreatment of membranes by soaking in aqueous isopropanol solutions. The benefits of this pretreatment are twofold: (1) After pretreatment, the membrane and the catalytic ink have similar solvent compositions, so that the membrane will not become wrinkled when the ink is subsequently applied; and (2) The membrane becomes very soft, so that the catalytic layer can integrate with the membrane more readily during the subsequent drying and hot-pressing steps.

As in the method described in the preceding article, the pretreated membrane is mounted in a frame. The membrane in the frame is laid down horizontally on a fine, absorbent, lint-free tissue to help control the rate of evaporation (as explained below) of volatile constituents (water and alcohols) of the ink to be applied next. The horizontal orientation is necessary to help ensure uniformity of the ink coating. The ink is then poured on the part of the membrane exposed in the aperture of the frame, and the ink is spread over the membrane by use of a glass rod.

Slow evaporation of the volatile constituents of the ink is necessary to obtain a crack-free catalytic coat on the membrane. Therefore, immediately after spreading of the ink, the membrane is placed in a polyethylene bag with a very small orifice for escape of the volatile constituents. After 24 to 48 hours, the coating is dry and the membrane can be taken through the hot-pressing process as in the method of the preceding article.

The performances of electrode structure made by a previous method and by the present improved method were evaluated in a laboratory fuel-cell apparatus at a temperature of 90 °C. In each case, a 1 molar aqueous methanol solution was circulated past the anode side, while air at 20 psig (gauge pressure of 14 kPa) was circulated past the anode. The measured performance of the improved version was superior; in particular, the peak power density of the improved version was 210 mW/cm², as compared to 160 mW/cm² for the previous version. Because of the greater power density, the weight of a fuel-cell stack could be reduced by about 25 percent without loss in performance.

This work was done by William Chun, Sekharipuram Narayanan, Barbara Jeffries-Nakamura, and Thomas I. Valdez of Caltech for **NASA's Jet Propulsion Laboratory**. *Further information is contained in a TSP [see page 1].*

In accordance with Public Law 96-517, the contractor has elected to retain title to this invention. Inquiries concerning rights for its commercial use should be addressed to

Technology Reporting Office
JPL
Mail Stop 122-116
4800 Oak Grove Drive
Pasadena, CA 91109
(818) 354-2240

Refer to NPO-19940, volume and number of this NASA Tech Briefs *issue, and the page number.*

Electric-Arc and Electrochemical Texturing of Surfaces

Potential applications include x-ray-tube anodes and orthopedic implants.

Lewis Research Center, Cleveland, Ohio

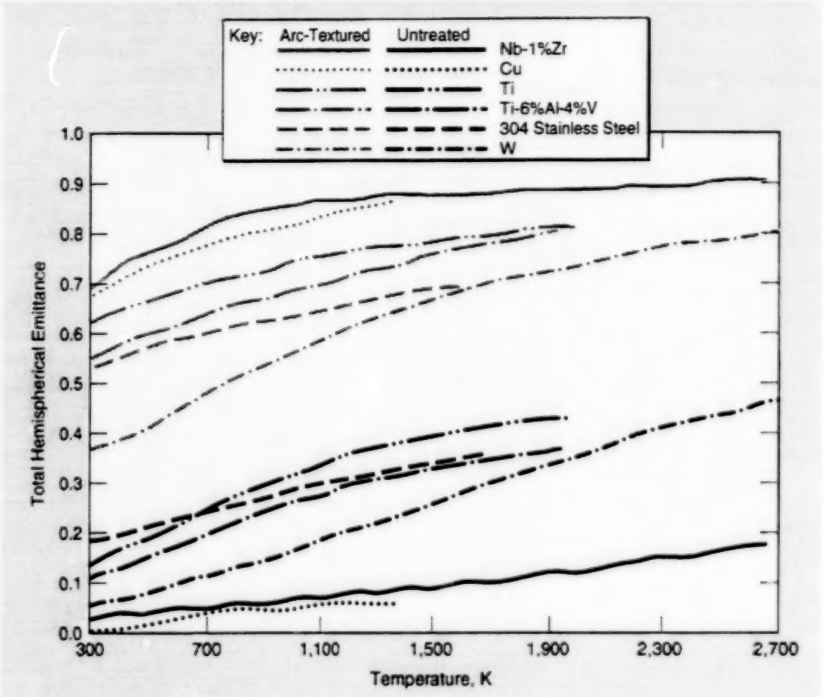

Figure 1. **Total Hemispherical Emittances** of specimens of several alloys were increased considerably by texturing with carbon arcs.

Electric arcs and electrochemical etching can be used to impart microscopic textures to surfaces of metals. In electric-arc texturing, one strikes an arc between a water-cooled electrode and a substrate that one seeks to texture. As the arc is moved across the substrate surface, a condensate from the plasma consisting of a mix of electrode and substrate species becomes redeposited on the substrate, forming an extremely rough surface layer that is intimately mixed with, and attached to, the substrate. The thermal emittances of arc-textured surfaces are considerably greater than those of the corresponding untreated surfaces. Unlike high-thermal-emittance oxide coatings, arc-textured surfaces are integral with substrates and are thus less likely to spall because of differential thermal expansion over wide ranges of operating temperatures. Arc texturing shows promise for enhancing the performances of metal components that must radiate heat; for example, anodes of x-ray tubes used in computer-assisted tomography, or waste-heat radiators on spacecraft.

Experiments in arc texturing were performed using (1) substrates made of various elemental metals and metal alloys; (2) electrodes made of carbon or silicon carbide; and (3) various arc currents, both dc and ac. The carbon electrodes were operated in argon; the silicon carbide electrodes were operated in air. Initial tests showed that ac arcs yielded higher emittances; thereafter, all texturing was done with sinusoidal-waveform ac arcs at (1) currents from 14 to 20 A with frequencies from 100 to 1,000 Hz in the case of carbon electrodes and (2) currents of 15 A with a frequency of 60 Hz in the case of silicon carbide electrodes. Figure 1 shows the increases in total hemispherical emittances of various alloy substrates, both untreated and treated by carbon-arc texturing.

In electrochemical texturing, a substrate is connected as the positive electrode in an electrochemical cell, and during operation of the cell, the electrolyte is agitated. The result of this process is a random distribution of electrochemically etched pits produced on the substrate surface. Experiments in electrochemical texturing were performed on substrate rods of the alloy Ti/6Al/4V (numbers indicate weight percentages, with balance of Ti), using an aqueous solution of sodium chloride as the electrolyte. The electrolyte was agitated by an ultrasonic-bath apparatus; the stainless-steel wall of the apparatus both contained the electrolyte and served as the negative electrode of the electrochemical cell. The agitation of the electrolyte assisted in the removal of oxides forming on the surfaces of the rods. In each experiment, only the end face of the rod was exposed, at a current density of 4.2 A/cm^2. The resulting erosion took the form of approximately hemispherical etch pits, with diameters of about 50 μm, randomly separated by unetched metal surface areas (see Figure 2).

Figure 2. **Etch Pits Separated by Unetched Surface** are clearly visible in this optical micrograph of specimen of electrochemically textured Ti/6Al/4V.

The sizes and density of the etched pits could be tailored to favor the in-growth of bone on the stems of an orthopedic implant. Because there would be no buildup of material on surface areas between etch pits, the outside dimensions of the orthopedic-implant stems would be unaffected by the electrochemical texturing. Thus, use of electrochemical texturing would not make it necessary to alter the dimensions of orthopedic implants.

This work was done by Bruce A. Banks and Sharon K. Rutledge of **Lewis Research Center** *and Scott A. Snyder of Ohio Aerospace Institute. Further information is contained in a TSP [see page 1].*

Inquiries concerning rights for the commercial use of this invention should be addressed to NASA Lewis Research Center, Commercial Technology Office, Attn: Tech Brief Patent Status, Mail Stop 7–3, 21000 Brookpark Road, Cleveland, Ohio 44135. Refer to LEW-16605.

Lead Bromide Crystals Doped With Silver Bromide

Doping suppresses cleavage, resulting in crystals of higher quality.

Lewis Research Center, Cleveland, Ohio

Doping with silver bromide has been found to be an effective technique for enhancing the optical homogeneity and other qualities of single crystals of lead bromide. These crystals are grown from melts by directional solidification. The doping suppresses cleavage that would otherwise occur during cooling after directional solidification.

Like other lead halides, silver bromide is potentially useful in acousto-optical and photoluminescent devices; the combination of optical and acoustical properties of the lead halides may be particularly suitable for extending the performances of optical signal-processing systems. Lead halides exhibit very high acousto-optical figures of merit; for example, the acousto-optical figure of merit of lead bromide is about 550 times that of quartz. Lead halides also exhibit a transparency range wider than that of most other commercially available materials that could be used for the same purposes.

To realize the full potential of lead halides, it is necessary to grow high-quality crystals without cracks. In the case of highly pure lead bromide, a second-order solid-state phase transformation occurs near the melting temperature during cooling after growth of a crystal from a melt. This phase transition changes the symmetry of the crystal, evolves a large amount of energy, and is associated with a disordering reaction. The resulting stress is large enough to cleave the crystal.

Doping with silver bromide reduces the energy of the phase transformation and thereby reduces the stress, making it possible to grow a crystal of better optical quality. Experiments have shown that doping to a level between 300 and 1,500 parts per million (ppm) is sufficient to prevent both microcracking and cleavage. Further experiments have shown that doping to a level as high as 3,500 ppm does not change acoustical or optical properties.

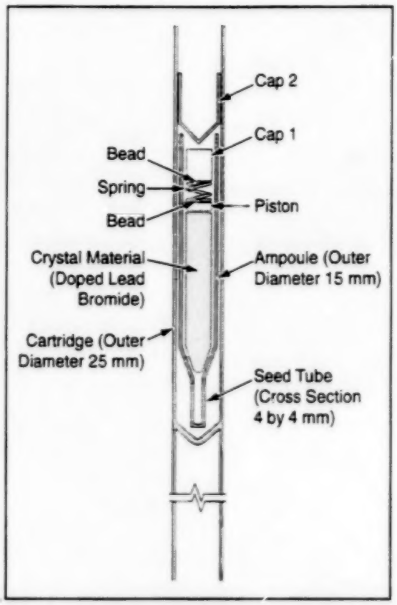

The **Ampoule and Cartridge** can be used to grow crystals of doped lead bromide by directional solidification in normal Earth gravitation or in microgravity. The spring-loaded quartz piston keeps the melt in contact with the seed.

The figure illustrates a quartz ampoule and cartridge designed to ensure proper seeding and vacuum conditions during growth of a crystal of doped lead bromide by the Bridgman directional-solidification technique. The top of the ampoule is sealed into the cartridge with cap 2. The bottom of the ampoule tapers down to a seed tube. Cap 1 seals the vacuum in the ampoule. To keep the melt in contact with the seed in the microgravity environment or in a tilted orientation in normal gravity, a spring pushes down on a quartz piston. The top and bottom ends of the spring are attached to cap 1 and the piston, respectively, via quartz beads. During the crystal growth, as the material melts and the volume changes, the spring force on the piston keeps the melt in contact with the seed.

The directional-solidification process can be implemented by translation of either the ampoule or the furnace used to melt the doped lead bromide contents along part of the length of the ampoule. The cartridge is suitable for either implementation. The dimensions shown in the figure are typical and can be changed to grow wider or narrower crystals. The lengths of the ampoule and cartridge can similarly be chosen to fit the length of the crystal to be grown.

This work was done by N. B. Singh, T. Henningsen, R. Mazelsky, M. Gottlieb, J. J. Conroy, R. H. Hopkins, Walter M. B. Duval, G. Santoro, Thomas E. Haley, and Ronald D. Hamacher of Westinghouse Electric Corp. for **Lewis Research Center**. *Further information is contained in a TSP [see page 1].*

Inquiries concerning rights for the commercial use of this invention should be addressed to NASA Lewis Research Center, Commercial Technology Office, Attn: Tech Brief Patent Status, Mail Stop 7–3, 21000 Brookpark Road, Cleveland, Ohio 44135. Refer to LEW-15539.

Thermal and Mechanical Effects in Graded Composite Cylinders

In this theory, coupling between microstructural and macrostructural effects is taken into account.

Lewis Research Center, Cleveland, Ohio

"HOTCFGM-1D" denotes a collection of four computer programs, plus the underlying theory, for calculating thermomechanical and inertial effects in axisymmetric cylindrical multiphase-composite-material objects that are functionally graded along their radial coordinates. The theory and programs are valid for the special case in which a thin cylindrical structural component is subject to macroscopically axisymmetric thermal and thermomechanical and inertial loads applied uniformly along its cylindrical axes.

The term "functionally graded" characterizes a class of materials, the microstructures of which are spatially graded to achieve specific thermal and/or mechanical properties. In the case of a multiphase composite material, functional grading can be effected by use of spatially variable spacing between individual fibers or other inclusions (see figure) and/or by use of inclusions of different properties, sizes, and shapes.

The "1D" in "HOTCFGM-1D" refers to the fact that the theory is a quasi-one-dimensional version of a more-general

higher-order theory, currently under development. The one-dimensionality is a consequence of the shapes of objects and symmetry of loading conditions described above. One aspect of this one-dimensionality is that the overall deformation of an object is characterized by a constant average axial stress and strain.

The one-dimensional higher-order theory was developed for use in the analysis, optimization, and design of axisymmetric cylindrical components of aircraft engines (e.g., combustor linings, rotor disks, and heat shields). The theory will enable designers to use functional grading to enhance the performances (e.g., deformation characteristics, resistances to thermal fatigue, and service lives) of such components. In the theory, coupling between microstructural and macrostructural effects in cylindrical bodies of revolution is explicitly taken into account for the sake of accuracy; in contrast, functionally graded objects cannot be analyzed accurately by following the older standard micromechanics approach based on the concept of representative volume-element mathematical models coupled with macrostructural-analysis models in a noninteractive manner.

The quasi-one-dimensional version of the theory includes representations of inertial body forces to account for effects of rotation. The theory also accounts for externally applied loads and radial temperature gradients. Applied loads and other boundary conditions can be in the form of temperatures imposed on the inner and outer surfaces, radial pressures, and/or radial displacements. The theory and computer programs can readily be modified by incorporation of constitutive theories of inelastic responses and of damage in constituent materials under nonisothermal conditions. At present, the computer programs include subprograms that implement the classical incremental theory of plasticity and the generalized viscoplasticity with potential structure (GVIPS) unified viscoplasticity theory.

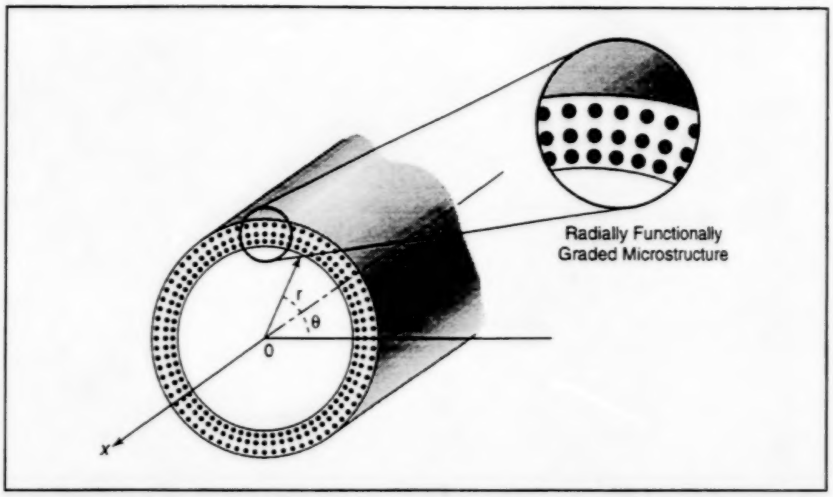

In the **Geometric Model of HOTCFGM-1D**, reinforcing phases are uniformly distributed in the axial and circumferential directions but arbitrarily distributed (for functional grading) in the radial direction. In this example, the reinforcing phases are axial fibers; in other examples, they could be circumferential fibers or discontinuous inclusions.

Three of the computer programs, called "fgmp.tube.f," "fgmp.homog.tube.f," and "fgm.gvips.tube.f," are research-oriented codes for investigating the effects of (1) functional gradings and (2) properties of multiphase reinforcements upon the temperature, stress, and inelastic strain field in thin shells subjected to axisymmetric thermomechanical and inertial loads. The user specifies the radial distribution of reinforcing material. The thermoelastic and inelastic properties of the individual phases can vary with temperature. The elastic phases can be isotropic; alternatively, they can be transversely isotropic with radial, circumferential, or longitudinal axes of symmetry. The inelastic phases can be modeled either by classical plasticity theory in fgmp.tube.f or GVIPS unified viscoplasticity theory in fgm.gvips.tube.f. A homogenization capability within fgmp.homog.tube.f admits the inclusion of heterogeneous phases.

The fourth computer program, called "fgmp.tube.opt.f," combines a major analysis module from fgmp.tube.f with a commercial optimization code called "DOT." The total optimization software package enables the user to identify radial distributions of reinforcing phases that minimize or maximize objective functions defined by the user; examples of such functions include internal moments or plastic strains.

This work was done by Marek-Jerzy Pindera of the University of Virginia and Jacob Aboudi of Tel-Aviv University for **Lewis Research Center**. *Further information is contained in a TSP [see page 1].*

Inquiries concerning rights for the commercial use of this invention should be addressed to NASA Lewis Research Center, Commercial Technology Office, Attn: Steve Fedor, Mail Stop 4–8, 21000 Brookpark Road, Cleveland, Ohio 44135. Refer to LEW-16753.

Improved Electrical Connections for Thin-Film Thermocouples

Unlike previous connections, these withstand high test temperatures.

Lewis Research Center, Cleveland, Ohio

Improved electrical connections have been developed for thin-film thermocouples used to measure temperatures on the surfaces of ceramic-matrix composite-material specimens during high-temperature tests. In a test, specimens are arranged in a four-sided configuration in a test rig, where they are heated from inside the rig by a flame. Composite specimens have endured up to 3,200 °F (1,760 °C) on the hot sides, while temperatures at electrical connections for thermocouples have reached 1,200 °F (650 °C). Previously, the electrical connections on the thermocouples could not withstand the test temperatures; they failed so frequently that no useful data could be taken. In addition, the design of the electrical connections made it difficult to change specimens in the test rig. The improved electrical connections withstand the test temperatures and make it possible to change specimens easily.

Thin-film thermocouples were installed on specimens by sputtering. Wires with a diameter of 5 mils (0.13 mm) were attached to the thermocouples by parallel-gap welding. Each specimen was

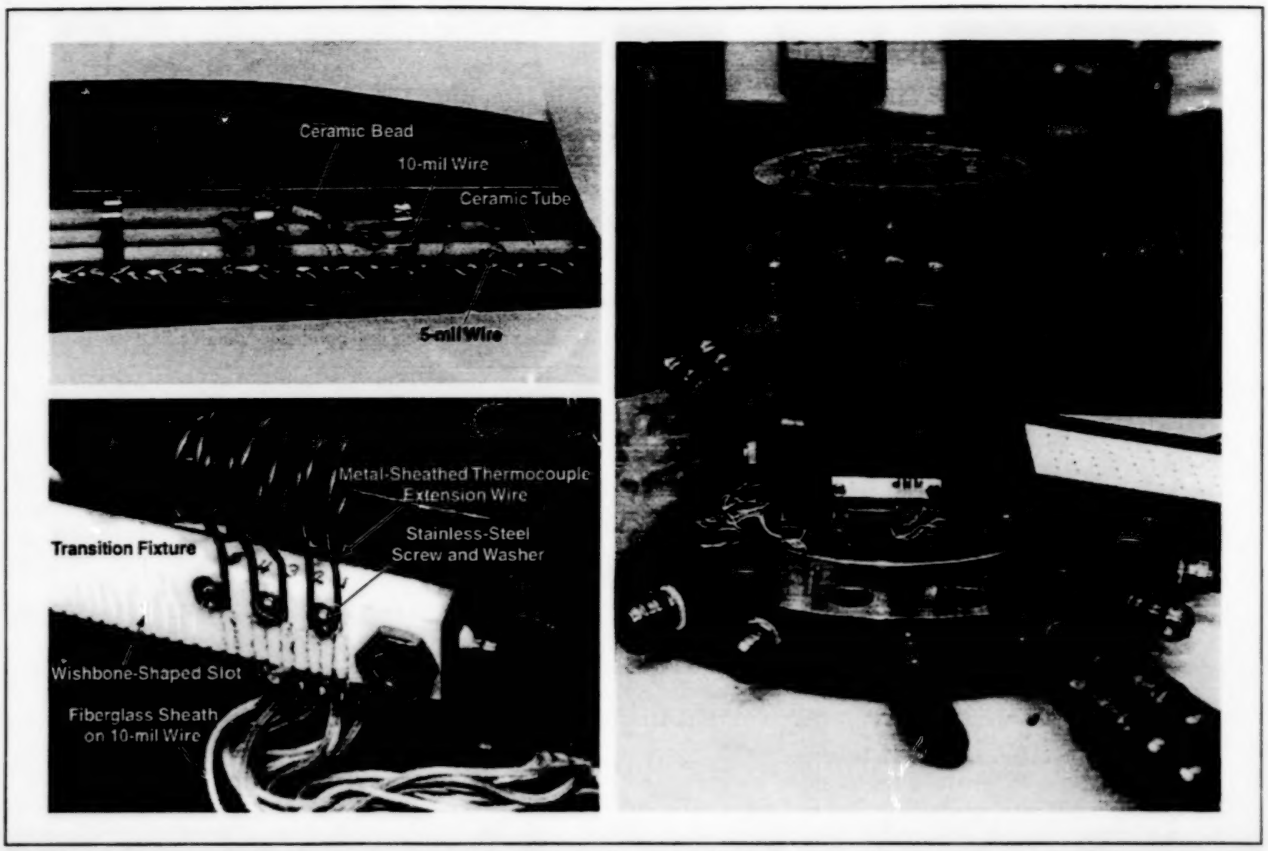

Electrical Connections for Thermocouples on a test rig withstand high temperatures. Thermocouples can readily be connected or disconnected at the transition fixture.

then mounted on a spring plate by use of straps made of a nickel alloy.

The figure illustrates key features of the improved electrical connections. Small ceramic tubes were strapped to the inside perimeter of the string plate. Wires with a diameter of 10 mils (0.25 mm) were run through the ceramic tubes. Starting from the outer ends of the ceramic tubes, the 10-mil wires were covered with fiberglass sheaths and run from the hot interior of the test chamber to a transition fixture (described in the next paragraph) located near the specimen, but, not so close as to be subjected to the maximum test temperature. At the inner ends of the ceramic tubes, the 10-mil wires were threaded through and bend around ceramic beads and attached to the 5-mil wires. The specimen as thus prepared was ready for installation in the test chamber.

The key to interchangeability of specimens was the transition fixture, which was made from a block of machinable ceramic. Small wishbone-shaped slots were milled into the block. A metal-sheathed thermocouple extension wire was stripped back and laid into the single-slot end of each wishbone, with its leads in the branch slots at the other end of the wishbone. In each branch slot, the thermocouple extension lead was placed in contact with the outer end of the corresponding 10-mil lead from the specimen. The metal-sheathed extension wires were held in place by washers and stainless-steel screws that engaged threads tapped into the block. Electrical contact between the thermocouple leads and the 10-mil specimen leads could easily be made and broken at the transition fixture.

This work was done by Chip Redding of **Lewis Research Center**. *No further documentation is available.*

Inquiries concerning rights for the commercial use of this invention should be addressed to NASA Lewis Research Center, Commercial Technology Office, Attn: Tech Brief Patent Status, Mail Stop 7–3, 21000 Brookpark Road, Cleveland, Ohio 44135. Refer to LEW-16688.

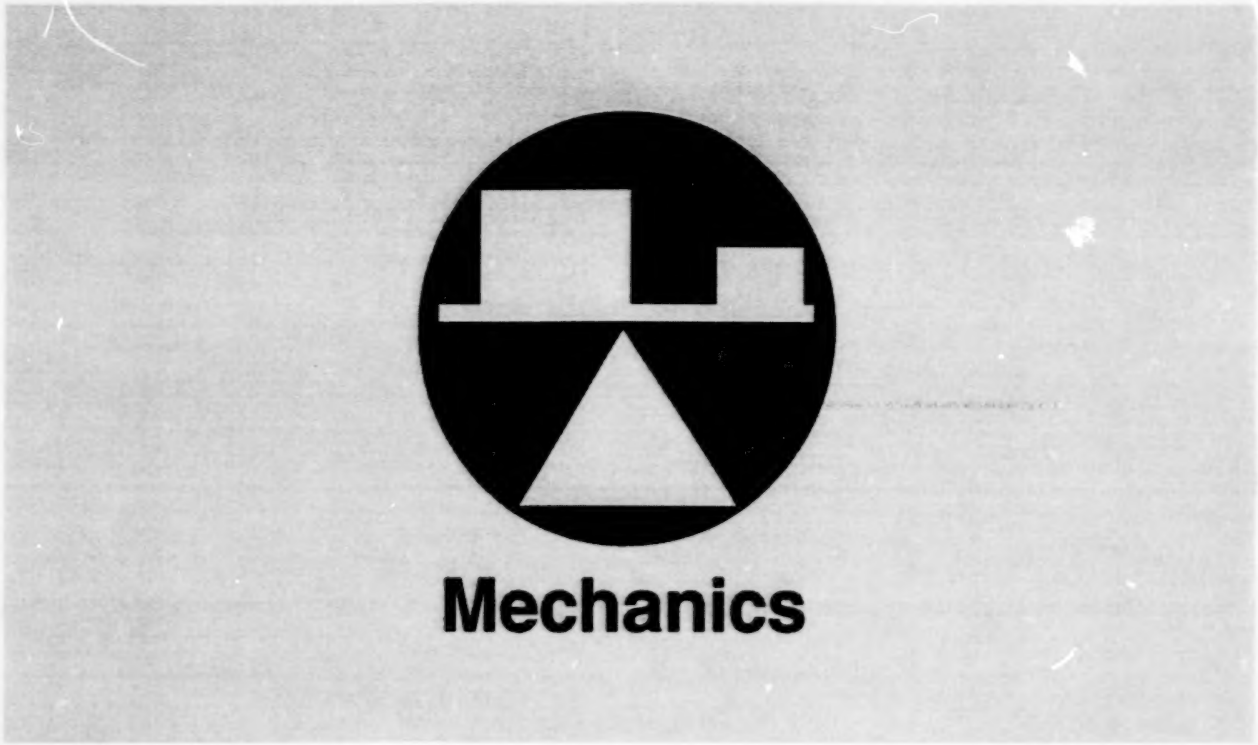

Mechanics

Books and Reports

39 Model-Based Monitoring for Spacecraft Thruster Leakage

BLANK PAGE

Model-Based Monitoring for Spacecraft Thruster Leakage

A report describes a method of detecting leakage in one of the 16 thrusters of the Cassini spacecraft. The detection method, implemented as part of the spacecraft flight software, is based on the fact that the three-axis rotational motion of a spacecraft is governed by the Euler's equation. The left-hand side of the Euler's equation contains both the inertia and gyroscopic torques, which are estimated by the attitude estimator of the attitude control software. The right-hand side of the Euler's equation contains reaction torques from both the thrusters and the reaction wheels which are also estimated. A residual angular-momentum vector, **R**, attributable to thruster leakage, is computed by taking the difference between the left- and right-hand sides of the Euler's equation and integrating this difference over time. When the absolute value of **R** grows beyond a preselected momentum threshold within a preselected time duration, then a leak is deemed to be present. The identity of a leaking thruster can also be determined using the polarities of the three components of the **R** vector. Once a leak is detected, remedial actions, such as the swapping of thruster branches could be made to stop the leak.

This work was done by Allan Y. Lee of **NASA's Jet Propulsion Laboratory**. *To obtain a copy of the report, "A model-based thruster leakage monitor for the Cassini spacecraft" see TSP's [page 1].*
NPO-20441

BLANK PAGE

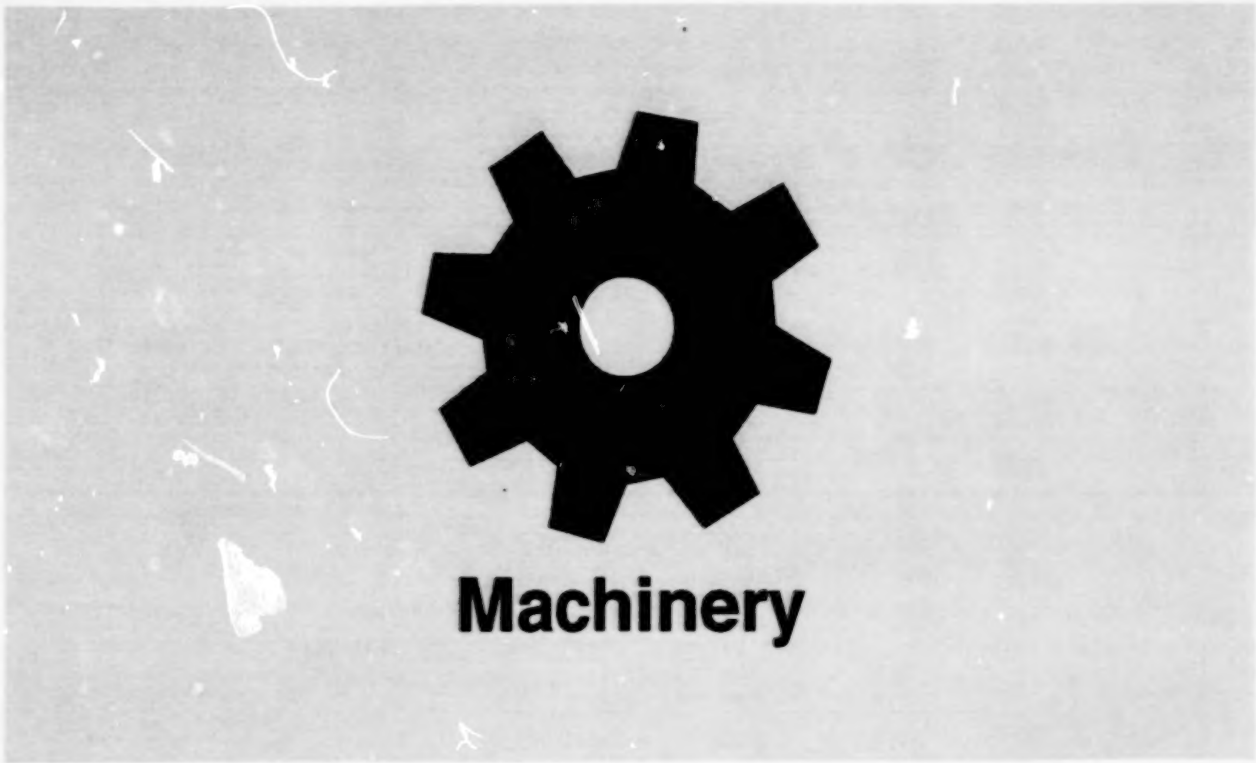

Machinery

Hardware, Techniques, and Processes

43 Human-Powered Centrifuges and Stationary Exercise Stations
44 Liquid-Circulation System Keeps Aircrew Members Cool
46 High-Altitude Flight Test of the Perseus B Airplane

BLANK PAGE

Human-Powered Centrifuges and Stationary Exercise Stations

Selectable modes of operation include constant speed, constant torque, and freewheeling.

Ames Research Center, Moffett Field, California

Human-powered machines that can be operated as centrifuges or as stationary exercise stations have been invented. These machines are suitable for a variety of terrestrial and outer-space applications that involve physical therapy, maintenance of physical fitness, centrifugal simulation of gravitation or acceleration, and/or measurement of physiological responses to exercise and centrifugation. A machine of this type can be operated in any of several selectable modes, in which one or more human participant(s) can be active or passive and in which the speed of rotation (and thus the centripetal acceleration), the human-generated torque, or the human-generated power can be regulated. Although the basic concept of human-powered centrifuges for such applications is not new, older designs for machines of this type do not provide for such a variety of operating modes.

One machine of this type (see Figure 1) includes recumbent seats for two riders on a turntable, plus a stationary seat near the turntable. A bicycle-type pedal-crank mechanism is located at each seat. The turntable can be powered by either or both riders and/or by a person on the stationary seat, by use of the bicycle-type mechanisms. Each bicycle-type mechanism includes a ratchet-type clutch to provide for freewheeling when the person using the mechanism elects not to pedal.

When rotated by human power, the pedals at either rider seat impart rotation to the turntable hub through a drive train that includes sprockets and chains that drive a pinion that meshes with a bevelled crown gear on the hub. Similarly, when rotated by human power, the pedals at the stationary seat impart rotation to the turntable hub through a drive train that includes sprockets and chains that drive a pinion that meshes with another bevelled crown gear on the hub.

Optional equipment includes a video camera, physiological monitoring equipment, and data-transmission equipment. Data from the monitoring equipment can be transmitted through slip rings and wires to an external computer system.

Figure 2 depicts a different machine of this type. For clarity of illustration, only one rider station is shown on the turntable, though in general there could be more than one. Also for the sake of clarity, the seat is not shown. As before, the rider supplies

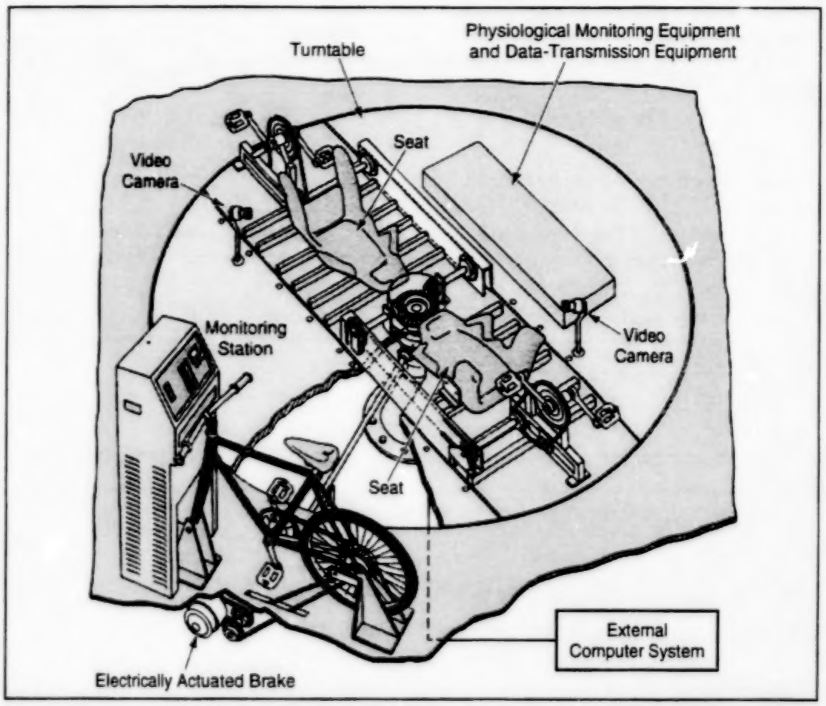

Figure 1. The **Turntable Can Be Powered** by two riders and/or by a person on a stationary bicycle-type mechanism. The electrically actuated brake resists the pedalling effort with a controlled torque.

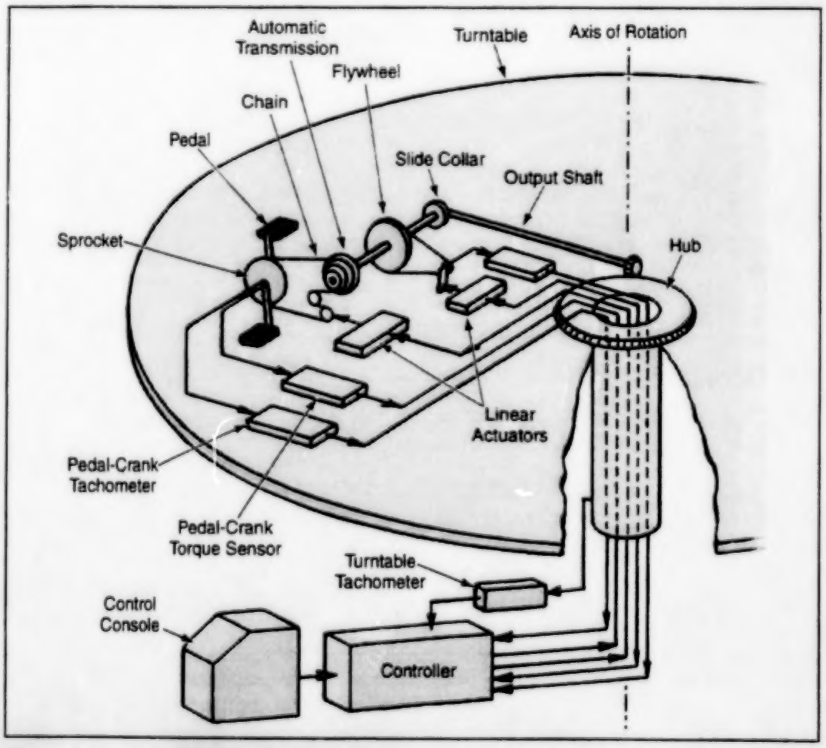

Figure 2. The **Control System of This Turntable** regulates the power demand on the rider, the torque applied by the rider, or the speed of rotation.

power via a bicycle-type mechanism. The pedal crank drives an automatic transmission that includes a ratchet-type clutch for freewheeling. The automatic transmission adjusts the gear ratio between the rider and the turntable and maintains constant rider power demand. The power output from the automatic transmission is sent through a flywheel friction brake and through a slide collar to the output shaft connected to the turntable hub. The slide collar is used, when needed, to disengage the output shaft to enable the rider to exercise while the turntable remains stationary. The flywheel friction brake is adjustable to absorb extra energy supplied by the rider and not needed to turn the turntable. The flywheel also provides smooth pedaling, especially when the output shaft has been disconnected for stationary operation.

A linear actuator changes gears in the automatic transmission in response to a command signal from a controller. Another linear actuator adjusts the tension on a strap on the flywheel, in response to another command signal from the controller. The controller is a programmable-logic control unit or other microprocessor device that is programmed to maintain a constant load on the rider, regardless of the speed of rotation. Control is maintained by using feedback from a pedal-crank torque sensor (load sensor) and a pedal-crank tachometer. The controller compares the preset commanded values (speed of rotation and load on the pedaling rider) to the actual values and responds by adjusting the tension on the strap and selecting the gear ratio on the automatic transmission.

The tension on the strap is measured and fed back to the controller, which then commands the second-mentioned linear actuator to adjust the tension. The output of a turntable tachometer is used as a feedback signal for regulating the speed of rotation and thus the centrifugal force, which can be preset and changed as desired prior to or during operation. The workload or power output required of the rider can be preset and maintained at a constant level independent of the speed of rotation. For operation at a constant speed of rotation, the turntable can be accelerated up to the preset speed but cannot be made to turn any faster, regardless of additional rider effort: this is accomplished through a feedback subsystem that causes excess power to be diverted to storage or dissipated.

This work was done by Gerald M. Mulenburg and Joan Vernikos of **Ames Research Center**. *Further information is contained in a TSP [see page 1].*

This invention has been patented by NASA (U.S. Patent No. 5,616,104). Inquiries concerning nonexclusive or exclusive license for its commercial development should be addressed to the Patent Counsel, Ames Research Center [see page 1]. Refer to ARC-12058.

Liquid-Circulation System Keeps Aircrew Members Cool

Flight-test pilots have expressed approval.

Dryden Flight Research Center, Edwards, California

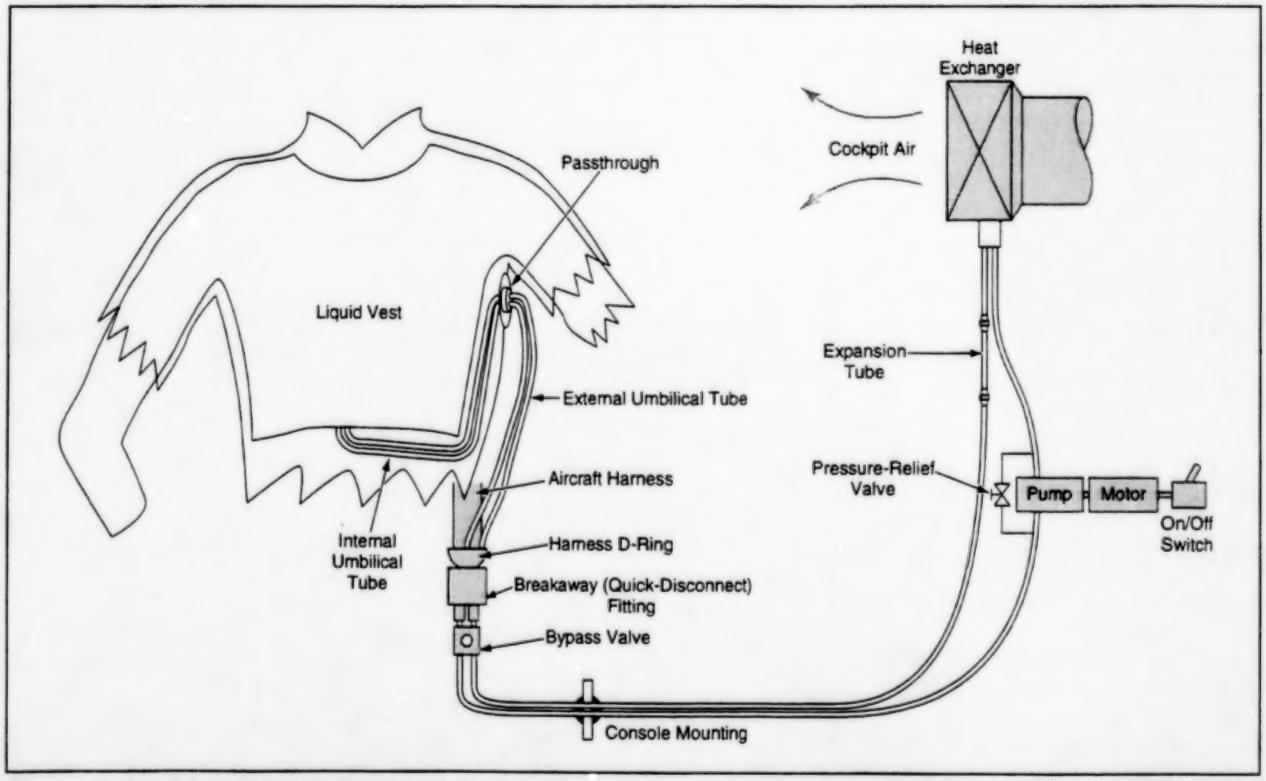

Figure 1. **A Heat-Transfer Liquid Is Circulated** between heat exchangers and a liquid vest to cool the wearer.

Each member of the aircrew of an advanced fighter airplane wears a complex, multilayered ensemble that imposes a significant thermal burden by inhibiting normal transport of heat from the body. The thermal burden may be aggravated by the use of nuclear, biological, and chemical (NBC) protective clothing, insolation through the canopy, psychological mission stress, and, in the future, positive-pressure breathing equipment used in COMBAT EDGE (Combined Advanced Technology

Pilot Wearing APECS Garment Under Flight Suit

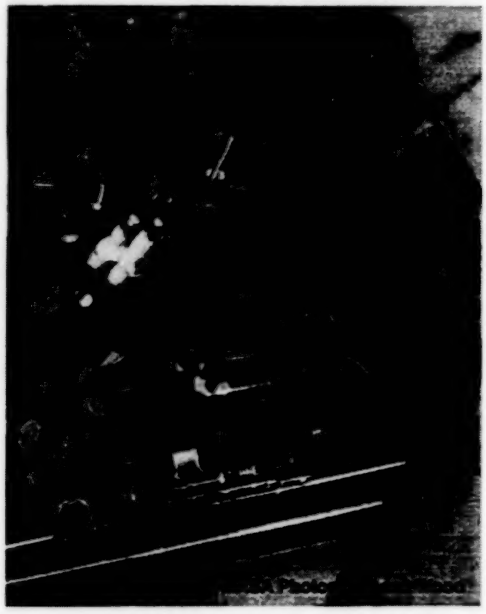

Quick-Disconnect Assembly

Figure 2. The **APECS Garment and Quick-Disconnect Assembly** are parts of the crew side of the APECS. The garment is worn under the flight suit. The quick-disconnect assembly is needed so that the APECS will not impede emergency egress.

Enhanced Design "G" Ensemble) equipped aircraft. The inability of the body to rid itself of excess heat can, at the very least, cause discomfort, but can also degrade mission effectiveness and pose a serious threat to safety and health. The aircrew personnel environmental control system (APECS) was designed to satisfy the need to remove excess heat from the body under these conditions. The APECS can also be used to keep pilots relatively cool when waiting for long times on the ground in hot weather, as well as in flight.

The APECS is a liquid-circulation cooling system (see Figure 1) that comprises two basic subassemblies — (1) the crew side, which is donned by each aircrew member, and (2) the aircraft side, which is permanently installed in each aircraft. The crew side (see Figure 2) consists of a cooling garment worn under the flight suit, tubing, and a quick-disconnect assembly for emergency egress. The aircraft side contains a network of plumbing, two heat exchangers, and a pump to chill and circulate the cooling fluid. The fluid consists of 70 percent distilled water and 30 percent denatured alcohol, plus a trace amount (150 parts per million) of sodium nitrate to inhibit corrosion in the pump. In future versions of this system, the pump will contain polytetrafluoroethylene gears, eliminating the need for sodium nitrate.

Figure 1 schematically depicts the APECS. The two heat exchangers in the aircraft side of the APECS are tied into the environmental control system (ECS) of the aircraft for cooling of the fluid. The fluid passes to thermal contact with the crewmember through tough nylon tubes worn close to the skin and, via thermal conduction, removes excess heat from the crewmember. The cycle is completed by pumping the heated fluid back to the heat exchangers for cooling. The temperature of the fluid pumped to the crewmember can be controlled manually by adjusting the cockpit air temperature via the ECS. During the winter, the heat-exchange process can be reversed by increasing the cockpit air temperature via the ECS, allowing warm fluid to pass through the APECS. The system includes a bypass that enables the crewmember to elect not to use the APECS while keeping cooled or heated fluid circulating in a standby mode.

The APECS hardware was originally designed and tested in the laboratory by Foster-Miller, Inc., of Waltham, Massachusetts under contract with the United States Air Force Flight Stress Protection Division of Armstrong Laboratories at Brooks Air Force Base. Human physiological testing to verify that the APECS would provide acceptable protection against heat stress was also conducted at Brooks Air Force Base. Having been proven in the laboratory, the APECS was then provided to NASA Dryden Flight Research Center for installation in an aircraft for field testing.

NASA elected to use the F-16XL aircraft as the test bed, inasmuch as this aircraft is flown by NASA as well as visiting Air Force Flight Test Center pilots. This gives the APECS exposure to a wide cross section of crewmembers with different physiological characteristics. To date, flight tests have proven the success of the APECS. Comments from aircrew members who have flown with the APECS indicate that the system works extremely well, is very comfortable, and responds quickly to changes in cockpit temperature. The system has operated during flight at high accelerations and during simulated air combat maneuvers, with no loss of cooling and without noticeable effect on the mobility of the pilot under acceleration load.

Although the APECS is now installed in the F-16XL only, work is in progress to put the APECS in a two-seat F-15 aircraft as well as in a single-seat F-18 aircraft at NASA Dryden Flight Research Center. Plans for the future also provide for the incorporation of a preflight cooler to help control body temperature on the ground and in the cockpit prior to connection of the crew side of the APECS with the aircraft side.

This work was done by Nick Kiriokos and Mark Collard of **Dryden Flight Research Center** *and Dan Fischbach of Foster-Miller, Inc.*

DRC-98-86

High-Altitude Flight Test of the Perseus B Airplane

Flawless aerodynamic, propulsion, and control performance were observed.

Dryden Flight Research Center, Edwards, California

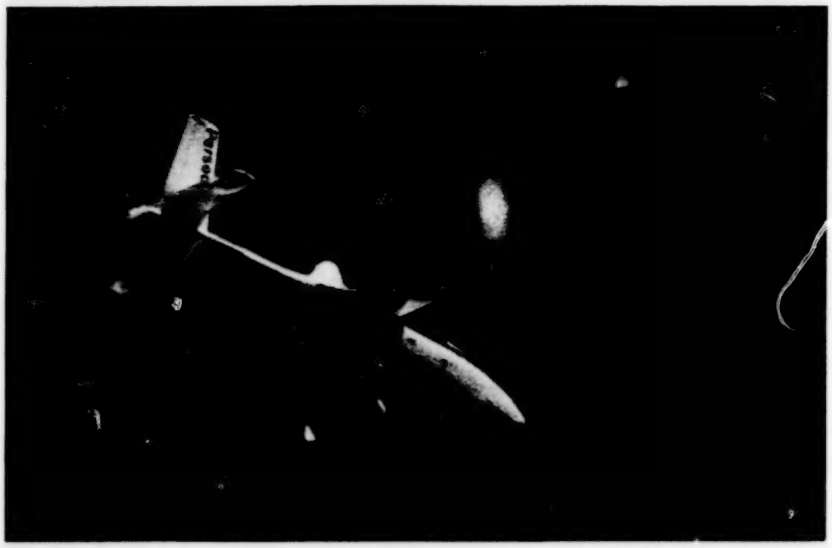

The Perseus B is a remotely piloted airplane designed to carry scientific instruments for research at high altitudes.

The Perseus B remotely piloted vehicle (RPV) has achieved a record altitude for a single-engine, propeller-driven airplane of 60,260 ft (18,367 m) on June 27, 1998. The Perseus B is one of the test-bed aircraft developed under NASA's Environmental Research Aircraft and Sensor Technology (ERAST) program for use in conducting high-altitude, long-duration missions carrying atmospheric sampling and sensing payloads for the scientific community within NASA and other agencies.

The Perseus B (see figure) is a slender, high-aspect-ratio airplane powered by a fuel-injected, four-cylinder ROTAX 912 engine aspirated by a three-stage, four-turbine turbocharger system with intercooling. Heat exchangers for the engine and intercooler coolant loops are a prominent feature on the center fuselage and under-wing positions. The engine is buried within the aft fuselage section, with a carbon-composite drive shaft extending rearward to drive a high-altitude, low-Reynolds-number-optimized two-blade propeller.

The airplane was demonstrated to fly at indicated airspeeds from 45 to 70 knots (23 to 36 m/s) and to climb at healthy rate of 200 ft/min (1 m/s) at an altitude of 60,000 ft (≈ 18 km). The ascent to this altitude takes about 170 minutes, corresponding to an average climb rate of about 350 ft/min (≈1.8 m/s).

Because of the developmental aspects of the flight, the maximum altitude was maintained only momentarily before descent was initiated. Temperatures encountered at altitude were as low as –70 °C, and proved too harsh for some components, including a Mode 3C Federal Aviation Administration radar transponder, which ceased operating at an altitude of approximately 53,000 ft (≈16 km), and began operating again at approximately 38,000 ft (≈12 km) after it had warmed sufficiently. Global Positioning System (GPS) data became intermittent above 57,000 ft (≈17 km), but because the GPS data stream returned upon descent through the same altitude, the intermittency is thought to be due to software lockout rather than thermal effects. Both of these anomalies are easily correctable by (1) adoption of better thermal management of the environment of the transponder (e.g., installation of a heating blanket), and (2) obtaining the correct GPS software for use at high altitude. The aerodynamic performance of the airplane and the performances of its propulsion and control systems were flawless throughout the flight.

Prior to the 60,000-ft flight, three other flights to altitudes of 15,000 ft (≈4.6 km), 27,000 ft (≈8.2 km), and 45,000 ft (≈14 km), respectively, were made as envelope-expansion missions. Data obtained from the total of four flights are being analyzed. The results of this analysis will be used to modify the aircraft to fly longer at 60,000 ft, as well as to increase the reliability and robustness of aircraft systems, including the data link and flight-control logic. These modifications will prepare the Perseus B aircraft for another flight-test phase to demonstrate the duration at altitude and mission-readiness of the aircraft and test team. Following this phase, it is expected that the aircraft will be ready for work in flying instruments and sensors for scientific missions.

The aircraft will be capable of carrying a nominal payload mass of 176 lb (80 kg) for 8 hours on station at 60,000 ft. It can carry as much as 265 lb (120 kg) on a mission of longer duration at lower altitude. Up to 1 kW of electrical power at a potential of 28 V can be provided to the payload.

The flight-test techniques developed and experience gained from this first Perseus B deployment will be utilized in improving the safety and efficiency of future flight-test programs for ERAST and other unpiloted-aircraft projects at Dryden Flight Research Center. Technical information is collected and used by all of the ERAST Alliance members to further the development and mission-readiness of high-altitude, long-duration uninhabited scientific aircraft.

This work was done by Aurora Flight Sciences Corporation and managed by Gary B. Cosentino for **Dryden Flight Research Center**. *Further information is contained in a TSP [see page 1].*
DRC-98-89

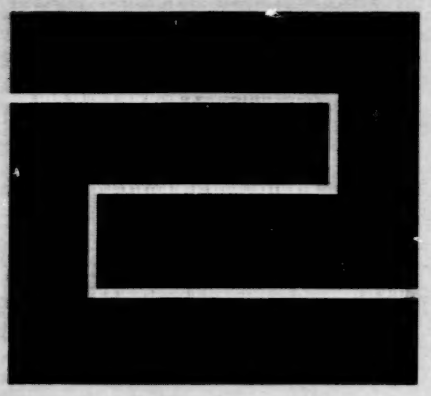

Fabrication Technology

Hardware, Techniques, and Processes

49 Software for Minimizing and Removing Burrs in Manufacturing

BLANK PAGE

Software for Minimizing and Removing Burrs in Manufacturing

The overall costs of manufacturing precise components would be reduced.

Lewis Research Center, Cleveland, Ohio

In a **Typical Use of the BurrEXPERT**, the user seeks to predict and minimize the burrs that would be formed in drilling intersecting holes in a block destined to become a valve body. As development continues, DEXTER (and eventually other software "experts") will be selectable from the menu.

An integrated suite of computer programs is undergoing development to address issues pertaining to the formation of burrs — undesired projections of metal that are generated on edges of workpieces in most metal-cutting operations. Burrs must be removed prior to assembly of machined workpieces, and therefore, plans for manufacturing must usually provide for deburring operations. The developmental software is intended to provide capabilities to (1) predict and minimize the formation of burrs and (2) plan deburring operations to maximize deburring performance and thereby reduce the overall cost of the design-to-fabrication cycles of precisely machined components.

One of the two main programs in this software system is called "BurrEXPERT." With the help of a commercial computer-aided-design (CAD) program as an interface, the BurrEXPERT accepts a drawing of a three-dimensional part (see figure) and assesses the burr-formation potential of the design features of the part under various manufacturing-process plans. The prediction capabilities are driven by a burr-property knowledge base and known burr relationships. These relationships are based on types of manufacturing processes, process parameters, properties of materials, and interactions among part geometries, tool geometries, and tool paths. By interactively and iteratively predicting the sizes, shapes, and locations of burrs, users can plan machining and edge-finishing processes, thereby shortening the design-to-fabrication cycle.

The other main program in this system is the Deburring Expert (DEXTER). When fully developed, the DEXTER will guide the user in selecting candidate edge-finishing processes, by use of a decision strategy driven by a deburring knowledge base. Using predicted observable burr attributes of a part, the DEXTER will match the capabilities and limitations of deburring processes to the characteristics of the part, the burrs on the part, and the desired edges on the part. The DEXTER will evaluate the overall applicability of the processes in the deburring knowledge base to the features on the part. Upon completion of its evaluation, the DEXTER will present a selection of candidate deburring processes. The user can then choose to examine still images, multimedia video images, and animations to obtain detailed information about each candidate deburring process.

Ultimately, the BurrEXPERT will be integrated with the DEXTER to form the Edge Finishing Master software package, so that

reasoning about strategies for the prediction and minimization of burrs can be integrated directly with reasoning about the burr-removal process. The Edge Finishing Master will thus serve as a "seamless" edge-finishing software tool for use by design and manufacturing engineers at all levels of integration between design and manufacturing functions, including the highest level of integration, where the outcome of manufacturing of parts is simulated during the design stage. High levels of integration between design and manufacturing will enable designers to perform computational simulations to achieve optimal balances between opposing metrics (e.g., surface finish vs. total cost of production).

This work was done by Julie M. Stein, Andrew Chang, and David Dornfeld of Integrated Constructs, Inc., for **Lewis Research Center**. *Further information is contained in a TSP [see page 1].*

Inquiries concerning rights for the commercial use of this invention should be addressed to NASA Lewis Research Center, Commercial Technology Office, Attn: Tech Brief Patent Status, Mail Stop 7–3, 21000 Brookpark Road, Cleveland, Ohio 44135. Refer to LEW-16622.

Mathematics and Information Sciences

Hardware, Techniques, and Processes

53 Diagnosing Rotating Machinery Using Spectral Distribution Functions
54 Neural-Network Modeling of Flow Properties of an Object
56 Algorithm Accelerates Solution of Digraph Reliability Models

BLANK PAGE

Diagnosing Rotating Machinery Using Spectral Distribution Functions

Spectral distributions of vibration signals can reveal changes indicative of damage.

Ames Research Center, Moffett Field, California

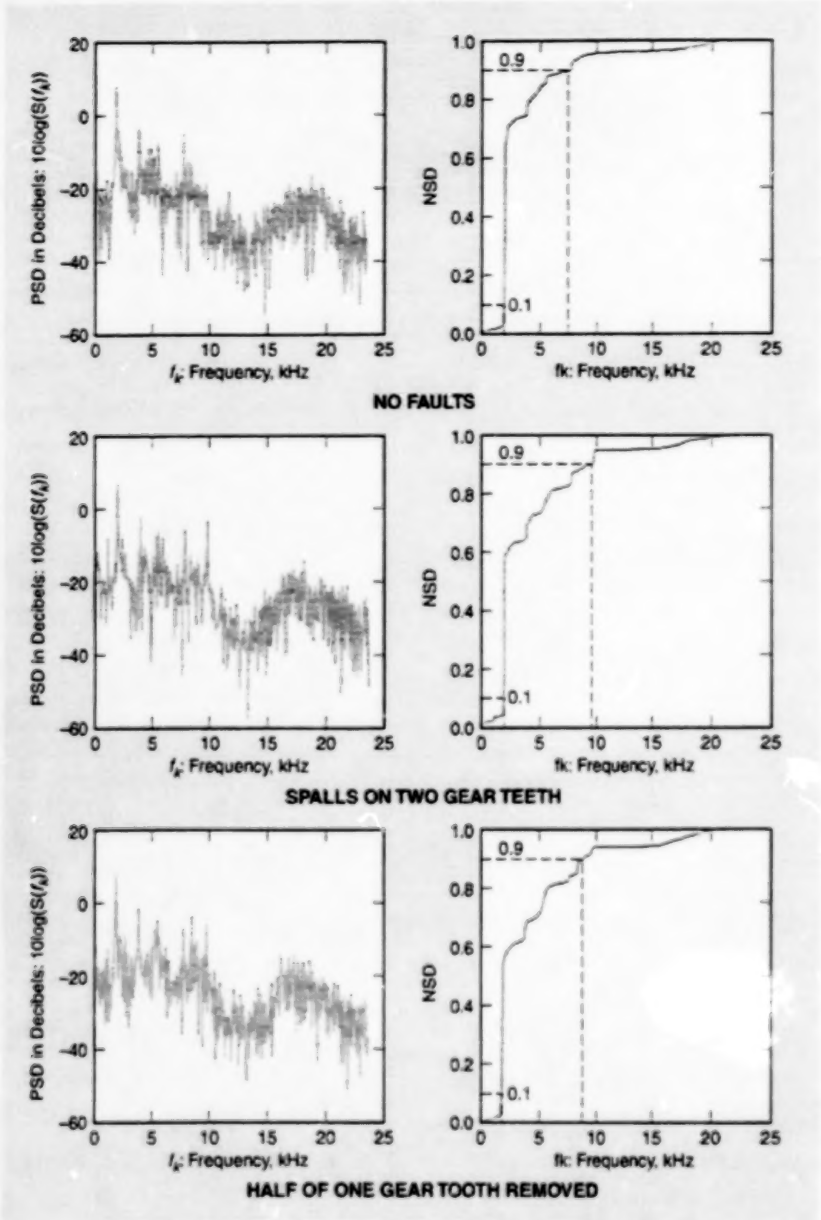

Figure 1. **PSDs and NSDs** were computed from vibration data acquired under three test conditions. Spectral changes associated with damage can be seen more easily in the NSDs than in the PSDs.

A method for detecting and characterizing faults in a rotating machine involves analysis of selected aspects of the evolution of the spectral distribution function (SDF) of its vibrations. The method is based on the proposition that long-term accumulation of damage (e.g., bearing wear or spalling of gear teeth) is accompanied by long-term changes in the SDF, and that these changes are revealed as differences among SDFs computed from short-observation-time vibration data. Data displays produced according to older vibration-analysis methods, including methods based on the conventional power spectral density (PSD), tend to display large components of random noise and other artifacts that often make interpretation difficult. The present method based on the SDF gives more robust indications of changes, yet entails little more computation than do methods based on the conventional PSD.

The SDF is derived from the PSD. It is a monotonically increasing function that bears the same relation to the PSD as a cumulative probability distribution to the probability density function.

Consider a vibration signal $X(t)$, where t is time. Let $X(t)$ be sampled at intervals of Δt to obtain the time series $X_j = X(j\Delta t)$, where j is an integer. Let the time series comprise a total of N samples. Let the time series be transformed as

$$C_k = \sum_{j=1}^{N} X_j e^{2\pi i(j-1)(k-1)/N}$$

for any integer k from 1 to N. The periodogram representation at $M = (N/2) + 1$ points is given by

$$S_k = \frac{C_k C_k^*}{N^2}$$

for $k = 1$ or M and

$$S_k = \frac{\left(C_k C_k^* + C_{N+2-k} C_{N+2-k}^*\right)}{N^2}$$

for any integer k from 2 to $M-1$, where the superscript asterisk denotes the complex conjugate. This representation is an M-line discrete estimate of the power spectral density, for frequencies $f_k = (k-1)/(N\Delta t)$.

The sum of all terms in the periodogram is the mean-square amplitude of the time series — a measure of the total signal energy. The spectral distribution function (SDF) in this situation is defined as the partial sum

$$F_k = \sum_{j=1}^{k} S_j$$

for any integer k from 1 to M. Thus, F_M is the mean-square amplitude, and F_k is an estimate of the energy at and below frequency $f_k = (k-1)/(N\Delta t)$. The SDF can be normalized by F_M, to obtain a normalized spectral distribution function (NSD) that is an estimate of the fraction of energy at and below a given frequency.

The method was applied in a test case involving vibration data from a helicopter tail-rotor gearbox. Data were taken under three conditions that might be encountered in a long-term progression of damage: (1) a baseline condition (no faults), (2) spalls on two gear teeth, and (3) half of

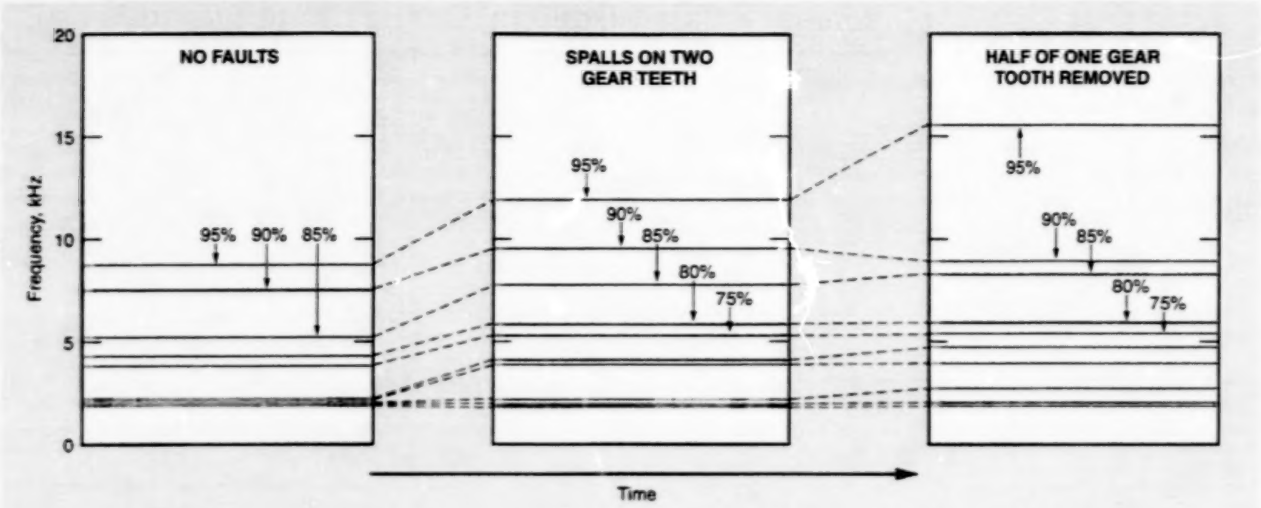

Figure 2. This **Contour Plot of Relative Energy Levels** was generated from the NSDs of Figure 1. Changes associated with damage can be seen even more easily than in the NSDs.

one gear tooth removed. For each test condition, the vibration measurements were digitized and phase-averaged with respect to shaft rotation, then N = 46,880 samples were acquired at a rate of 46,880 Hz (thus making the observation time 1 second).

Figure 1 shows the PSDs and NSDs for the three test conditions. The PSDs are characterized by a few tones rising above background noise. Although there are differences among the PSDs, they are difficult to identify by casual visual inspection. The differences among the NSDs are more obvious and are easily quantifiable. The discrete jumps in the NSD indicate the tones, while the finite-sloped portions indicate the buildup of frequency-dependent continuous random noise.

The quantifiable indicators in the NSD are the frequencies that bound specified relative energy levels; for example, the first and ninth deciles are marked by the dashed lines in Figure 1. A more meaningful way to display these indicators is to juxtapose and join plots of the frequencies, parameterized by the relative energy levels, for sequential observation times. The resulting combination of plots (see Figure 2) amounts to a contour plot of constant relative energy levels in frequency-time space. Such contour plots are simple and easy to read, and can be stored for use in subsequent diagnoses.

This work was done by Sanford Davis of **Ames Research Center**. *Further information is contained in a TSP [see page 1].*

This invention is owned by NASA, and a patent application has been filed. Inquiries concerning nonexclusive or exclusive license for its commercial development should be addressed to the Patent Counsel, Ames Research Center [see page 1].

Refer to ARC-14240.

Neural-Network Modeling of Flow Properties of an Object

Wind-tunnel testing time can be reduced.

Ames Research Center, Moffett Field, California

A method of computational simulation of the aerodynamic- or hydrodynamic-flow performance features of objects involves the use of neural-network mathematical models implemented in computer hardware and software. The method can be applied in conjunction with wind-tunnel, water-tunnel, or water-trough testing of scale models of such diverse objects as aircraft or parts of aircraft, sails, fins, turbine blades, and boat hulls.

In the case of an aircraft, for example, a neural network can be trained from (1) test input signals (e.g., positions of control surfaces; angle of attack; angles of roll, pitch, and yaw; power settings; and airspeed) and (2) test output signals (e.g., lift, drag, pitching moment, and/or other performance features). In general, the relationships between the input and output variables are nonlinear. The present method harnesses the ability of neural networks to learn nonlinear relationships between input and output variables.

A neural-network model can be used to perform the nonlinear interpolation or extrapolation needed to predict the output variables for previously untested combinations of input variables. Moreover, the neural-network model can be generated during a wind-tunnel test, and its predictions used immediately to focus the test conditions on input-variable combinations that have the greatest engineering significance; for example, the predictions can be used to "zero in" on control-surface settings that result in maximum lift. Thus, the method can reduce wind-tunnel test time, which can be expensive (≈$6,000/h in a large wind tunnel).

The figure illustrates the application of the method to a subset of the aerodynam-

ic characteristics of a model airplane in a wind tunnel. The neural network includes an input layer containing three nodes (one for each of three input variables), a hidden layer containing 15 nodes, and a single output node. The input variables are the angle of attack, the leading-edge flap position, and the trailing-edge flap position. The output variable could be the coefficient of lift (C_L), the coefficient of drag (C_D), the coefficient of pitching moment (C_M), or the lift-to-drag ratio (C_L/C_D). This neural network is a relatively simple one, chosen for the sake of clarity in illustrating the method; in a practical application, there could be more than three input nodes and variables, more or fewer than 15 hidden nodes, and multiple output nodes and variables.

Each hidden node is connected to the output node and to the input nodes. The signal transmitted along each connection is proportional to a weight or strength (which is represented in software as one of the elements of a weight matrix). Thus, the input to each hidden node is a weighted sum of the outputs of the input nodes, while the input to the output node is a weighted sum of the outputs of the hidden nodes. The output of each node is a function (denoted an "activation function) of its input; typically, the activation function is a sigmoid function like a hyperbolic tangent. A neural-network module in the software implements the activation function.

In the training process, the neural network is presented with sets of input variables and corresponding output variables from wind-tunnel tests. The connection weights are adjusted in an iterative subprocess in an effort to make the neural-network outputs approach the correct values of the output variable.

The learning problem to be solved in the iterative subprocess can be characterized as an optimization problem: One seeks connection-weight values that are optimum in the sense that they minimize some measure of the error in the neural-network outputs; e.g., the sum of squares of the differences between the neural-network outputs and the correct values of the output variable for all training sets. If training set is relatively small (no more than a few hundred data points), the learning problem is best solved by the Levenberg-Marquardt method. The training process is terminated when the error measure falls below a specified low level or a specified maximum number of iterations is exceeded.

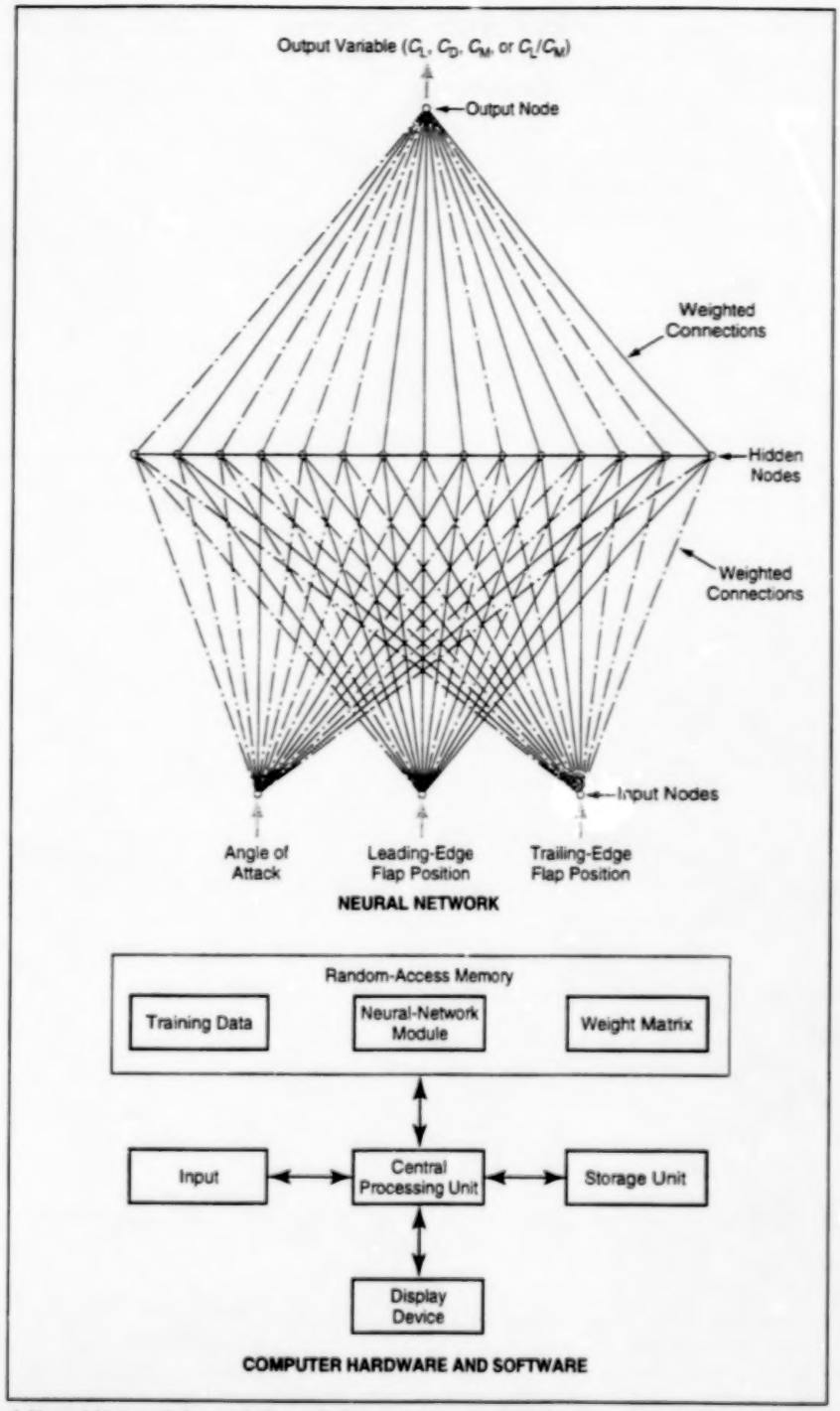

A Neural Network for modeling selected aerodynamic characteristics of an airplane is implemented in computer hardware and software.

This work was done by Charles Jorgensen and James Ross of **Ames Research Center**. *Further information is contained in a TSP [see page 1].*

This invention has been patented by NASA (U.S. Patent No. 5,649,064).

Inquiries concerning nonexclusive or exclusive license for its commercial development should be addressed to the Patent Counsel, Ames Research Center [see page 1]. Refer to ARC-14008.

Algorithm Accelerates Solution of Digraph Reliability Models

Computing times are reduced from days to minutes.

Ames Research Center, Moffett Field, California

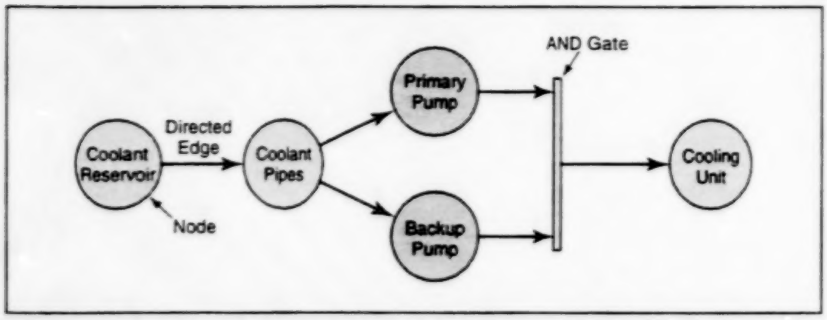

Figure 1. This Is a **Digraph (Directed-Graph) Representation** of reliability of a cooling system. Each node (circle) represents a failure in a component of the system. Each directed edge represents both a flow of coolant and a path of propagation of failure. The vertical bar represents an AND gate, which is used here because both the primary and backup pumps must fail in order for the cooling unit to fail for lack of coolant.

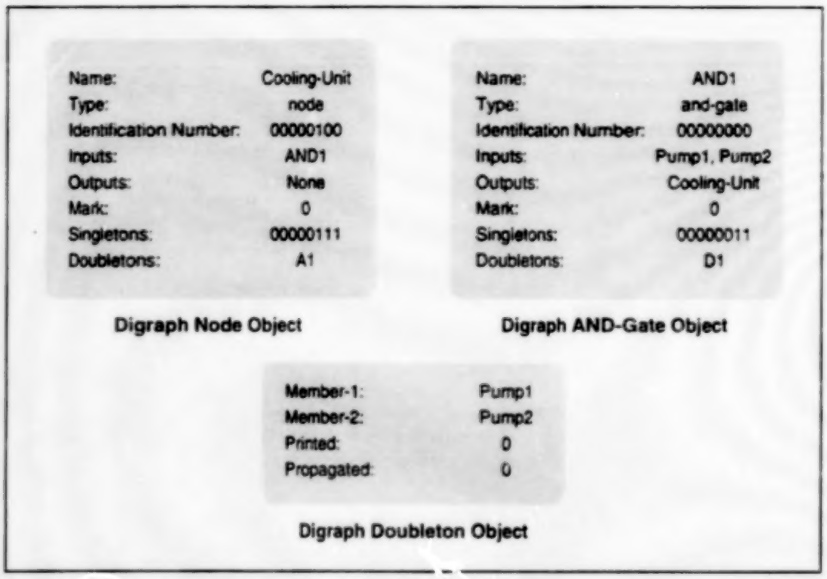

Figure 2. **Nodes and AND Gates** are represented by programming objects that contain data on identity, condition (failed or not failed), and connectivity.

The SourceDoubls algorithm efficiently solves for singletons and doubletons of a digraph reliability model (defined below). In the case of a complex system of hardware and/or software represented by a correspondingly complex digraph reliability model, it can take as long as days to compute the solution by older, matrix-based methods. In contrast, SourceDoubls finds the solution in minutes, opening the possibility of using a digraph model for real-time monitoring and diagnosis of the system.

A digraph model (see Figure 1) is a graphical combinatorial failure-space model of a system, comprising nodes and AND gates connected by directed edges. Each node represents a piece of hardware or software, a mode of operation, a human action, or other component or aspect of the system wherein a failure could occur. Each directed edge represents a physical connection and/or functional dependence through which the occurrence of a failure can flow through the system to cause failure at another node. If a node is marked "failed," then the failure is deemed to propagate along the output edge(s) of the node to any connected node(s). The model can include directed loops that represent cycles. The model can be derived fairly straightforwardly from a schematic diagram of the system augmented by knowledge about the design of the system and modes of failure of components.

A common operation performed on a digraph model is the calculation of single failures and pairs of failures that could cause a target failure event to occur. A single failure that causes the target failure event is called a "singleton" of that event. Two failures that combine (as represented by use of an AND gate) to cause a target failure event are said to constitute a "doubleton" of that event. Finding singletons and doubletons for a digraph model is useful for finding weak links in the system and for quantitative estimation of the reliability of the system. Singleton and doubleton solutions can also be used in diagnosing the system because they indicate possible causes of failure events.

The SourceDoubls algorithm solves for the singletons and doubletons of all the nodes in a digraph model of a system by use of object-oriented programming concepts (see Figure 2). Each node, AND gate, singleton, or doubleton is stored as an object in computer memory. Each node or AND-gate object includes a number of slots to represent such data as the identity of the object, its input(s) and output(s), and its singleton(s) and doubleton(s). One of the slots is the mark slot, which contains a datum (1 or 0) that indicates whether a failure has or has not propagated to the node or AND gate. The input and output slots contain lists of pointers to nodes and AND gates directly connected to a given node or AND gate. The singletons slot contains information on the identities of the nodes associated with singletons of the given node, while the doubletons slot contains a list of pointers to doubleton objects. A doubleton object contains slots that point to the two nodes (objects) that are members of the doubleton, plus flags that indicate whether information on the doubleton has been printed or processed yet.

SourceDoubls finds singletons and doubletons in source operations:

- In the case of a singleton, a node of interest is marked as failed and the mark is propagated through the directed edges of the digraph to determine which other nodes can be expected to fail as a result. The node of interest is thus determined to be a singleton of each of the other failed nodes. The singleton calculations are completed before starting the doubleton calculations.
- The doubletons of a given node are

found by searching for the doubletons for all the AND gates directly upstream of the node. This is accomplished in a limited source operation on each AND gate in the digraph. In this operation, the mark is allowed to travel only to nodes and not through AND gates. After this operation, the AND gate is added to the list of upstream AND gates of each node that the mark reached in the operation. The foregoing description is simplified for the sake of brevity. The algorithm also includes provisions for finding hidden doubletons, increasing computational efficiency by avoiding redundant calculations, and avoiding infinite computational loops when cycles are encountered.

This work was done by D. L. Iverson and F. A. Patterson-Hine of **Ames Research Center**. *Further information is contained in a TSP [see page 1].*

Inquiries concerning rights for the commercial use of this invention should be addressed to the Patent Counsel, Ames Research Center [see page 1]. Refer to ARC-12071.

END

DATE FILMED

07-02-99